Journal of
Materials Chemistry B

Materials for biology and medicine

Accepted Manuscript

This article can be cited before page numbers have been issued, to do this please use: X. Y. Xuan, M. Qian, L. Pan, T. Lu, L. Han, H. Yu, L. Wan, Y. Niu and S. Gong, *J. Mater. Chem. B*, 2020, DOI: 10.1039/D0TB01657H.

ROYAL SOCIETY OF CHEMISTRY

rsc.li/materials-b

View Article Online
DOI: 10.1039/D0TB01657H

Journal Name

ARTICLE

Longitudinally Expanded Ni-Based Metal-Organic Framework with Enhanced Double Nickel Cation Catalysis Reaction Channels for Non-Enzymatic Sweat Glucose Biosensor

Received 00th January 20xx,
Accepted 00th January 20xx

DOI: 10.1039/x0xx00000x

www.rsc.org/

Xiaoyang Xuan[a, c], Min Qian[a, *], Likun Pan[b, *], Ting Lu[b], Lu Han[b], Huangze Yu[b], Lijia Wan[b], Yueping Niu[a, c], Shangqing Gong[a, c, *]

Nickel-based metal-organic frameworks (Ni-MOFs) have attracted increasing attention in non-enzymatic glucose sensing. However, the insufficient active Ni cation sites from stacked MOF layer, the unclear Ni catalysis mechanism, and the severe liquid alkaline electrolyte remain challenging for practical applications. In this work, the sonication-induced longitudinal-expansion of Ni-MOFs increases the active nickel ion sites, which not only enhances the current response to glucose detection, but also shows the oxidation peak evolution of nickel ions with different sonication time, revealing the mechanism of different glucose detection channels. The Ni-MOF sonicated for 60 min (60 min Ni-MOF) displays enhanced Ni(III)/Ni(II) and more significant Ni(IV)/Ni(III) double nickel cation channels for catalyzing glucose into glucolactone compared to 0 min Ni-MOF (without sonication), showing optimized glucose detection ability with a high sensitivity of 3297.10 μA $mM^{-1}cm^{-2}$, low detection limit of ~8.97 μM (signal-to-noise = 3) and wide linear response range from 10 to 400 μM from the cyclic voltammetry test as well as a high sensitivity of 3.03 μA mM^{-1} cm^{-2}, low detection limit of ~1.16 μM (signal-to-noise = 3) and wide linear response range from 10 to 2000 μM from the chronoamperometry test, respectively. More importantly, an all-solid-state glucose biosensor using a PVA/NaOH solid-sated electrolyte and a disposable 60 min Ni-MOF working electrode is assembled for non-enzymatic sweat glucose detection.

1. Introduction

Diabetes patients are suffering from invasive blood tests several times a day to monitor glucose concentrations using traditional blood glucose meter.[1,2] As human sweat contains glucose with a concentration from 5.6 to 2200 μM which is statistically related to blood glucose concentration,[3,4] recent research frontier has been focused on noninvasive glucose detection in sweat mainly in terms of enzymatic and non-enzymatic glucose detection. Karpova et al. developed a flow-through glucose biosensor based on Prussian blue and glucose oxidase,[1] and Zhao et al. reported an Au/Prussian Blue/glucose oxidase/chitosan glucose biosensor.[5] However, the key component enzyme in enzymatic glucose sensor has several disadvantages, such as high cost and complicated immobilization process, which is easy to lose activity and seriously affected by environmental conditions.[6-8] Non-enzymatic glucose detection is mainly based on the current response of directly oxidizing glucose molecules by non-precious transition metals, which is relatively low cost, simple, and stable.[9,10] Among various transition metals, Ni-based nano-materials, such as nickel metal,[11,12] nickel oxide,[13,14] and nickel hydroxide,[15] are typical non-enzymatic electrocatalysts for glucose detection,[16] and have been widely applied in non-enzymatic glucose sensing with good catalytic performance.[9,10,17,18]

Metal-organic frameworks (MOFs) composed of metal ions or clusters and polytopic organic linkers are important raw materials for making functional materials and have been applied in many fields. MOFs have been utilized as precursors for synthesizing catalysts.[19-21] Liao et al. reported a MOF precursor for generating an active interface between metal and oxide.[19] Chueh et al. summarized MOF-based bandgap materials for photovoltaic devices.[22,23] MOFs are also promising precursors for preparing functional carbons.[24-27] Because MOFs display large specific surface area and rich metal ion centers which can provide lots of active sites for glucose catalysis, they are broadly used in catalysis and sensing.[28-31] Xiao et al. reported a glucose sensor using ultrathin Ni-MOF nanobelts with a sensitivity of 1.542 μA mM^{-1} cm^{-2} and a linear range from 1 to 500 μM.[32] Wang et al.

[a] Department of Physics, School of Science, East China University of Science and Technology, Shanghai, 200237, People's Republic of China. E-mail: mqian@ecust.edu.cn
[b] Shanghai Key Laboratory of Magnetic Resonance, School of Physics and Electronic Science, East China Normal University, Shanghai, 200062, People's Republic of China. E-mail: lkpan@phy.ecnu.edu.cn
[c] Key Laboratory for Ultrafine Materials of Ministry of Education, Shanghai Engineering Research Center of Hierarchical Nanomaterials, School of Materials Science and Engineering, East China University of Science and Technology, Shanghai, 200237, People's Republic of China. E-mail: sqgong@ecust.edu.cn
Electronic Supplementary Information (ESI) available: [details of any supplementary information available should be included here]. See DOI: 10.1039/x0xx00000x

synthesized a glucose sensor using layer-assembled flower-like Ni-MOF/carbon nanotubes composite with a sensitivity of 77.7 μA mM^{-1} cm^{-2} and a linear range from 20 μM to 4.4 mM.[33] These works show the feasibility of Ni-MOF layered structure for effectively detecting glucose. However, the Ni-MOF layers used are often stacked together, which limits their exposed surfaces and active nickel ion sites, and great efforts are still necessarily devoted to further improving their detection sensitivity. Surface morphology control has been reported to provide more exposed active elemental sites.[34] Li et al. reported the in-situ growth of NiCo-MOF nanosheets on nano-porous gold substrates to prepare vertical arrays, where the active Ni and Co sites were sufficiently exposed, showing a high sensitivity to glucose of 684 μA mM^{-1} cm^{-2} and a linear range from 1 μM to 8 mM.[35] Unfortunately, the conductive gold substrate is expensive and involves complex surface treatment processes.[35,36] Ultrasonic-assisted exfoliation is a convenient and cheap method to improve the exposed surface and active site of materials, and has been widely used in the field of energy storage, catalysis, and sensor for material morphology regulation.[37] Yan et al. synthesized an accordion-like Ni-MOF with large exposed surface via ultrasonic treatment for supercapacitor, and a high specific capacity of 988 F g^{-1} was achieved.[38] Munonde et al. synthesized a NiFe layered double hydroxide on carbon black for oxygen evolution reaction (OER) and employed ultrasonic exfoliation for exposing more cationic active sites, showing that an exfoliated sample display ed a higher OER activity with an overpotential of 220 mV compared to 280 mV of a bulk sample at a current density of 10 mA cm^2 in an alkaline solution.[37] Lee et al. synthesized a SnS_2 nanoplate-decorated multi-walled carbon nanotube electrode for glucose sensor and conducted a ultrasonic treatment, where an exfoliated SnS_2 nanoplate-decorated electrode showed a higher sensitivity of 28.9 μA mM^{-1} cm^{-2} and a broader linear range from 62.5 μM to 2.8 mM while an unexfoliated sample only showed a sensitivity of 18.5 μA mM^{-1} cm^{-2} and a linear range from 250 μM to 1.5 mM.[39] Therefore, ultrasonic treatment should be effective to enrich the active sites of lamellar-structured Ni-MOF for glucose detection, but few investigations have been reported yet.

The redox reaction of Ni-based material to catalyze glucose is generally explained as deprotonation and isomerization of glucose by the Ni(III)/Ni(II) redox couple. Hwang et al. systematically summarized recent works on non-enzymatic glucose sensors in their review article and mentioned that Ni(III)/Ni(II) is often considered as the channel for glucose-catalyzed reaction with typical oxidative peaks at potentials of 0.2~0.4 V (vs. Ag/AgCl).[10] Toghill et al. summarized in a review article that a Ni(III) oxyhydroxide species is the catalytic component for nickel-based non-enzymatic glucose catalysis.[16] From the theoretical potential-pH diagram for the Ni-H_2O system, the valence state of nickel cation increases from Ni(II) to Ni(IV) gradually with increasing potential values, and cyclic voltammetry (CV) tests have been effectively applied for experimentally observing Ni(II)/Ni(III) and Ni(III)/Ni(IV) couples.[40,41] Rahmanifar et al. observed two redox peaks in the CV curves of Ni-MOF supercapacitors as Ni(II)/Ni(III) and Ni(II)/Ni(IV) redox couples at ~0.43 and ~0.47 V in 6 M KOH.[42] The observation of separated oxidation peaks in nickel based electrochemistry is important, as generally transition metal cation with higher valence state and smaller cation radius shows stronger oxidation activity.[43,44] Gao et al. revealed that a higher oxidation-state γ-phase Ni(IV) exhibited an enhanced OER property with a smaller overpotential of 0.331 V compared to 0.444 V of a lower oxidation-state β-phase Ni(III) for obtaining a current density of 10 mA cm^{-2}.[43] Bediako et al. found that an increase of γ-phase Ni(IV) with a higher average oxidation state of +3.6 in a nickel-borate catalyst film by anodization process helped to improve the electrocatalytic activity of OER compared to β-phase Ni(III) with a lower average oxidation state of +3.[44] Leem et al. showed that a high valence-state Ni(IV) was reduced to a low valence-state Ni(II) via two consecutive one-electron transfer channels of Ni(IV)/Ni(III) and Ni(III)/Ni(II) at 0.44 and 0.37 V, where the two-channel process helped to increase the total number of molecules being catalyzed and the catalytic efficiency, and a high OER current density of 10 mA cm^{-2} at 1.0 V was achieved.[45] Therefore, exploring the mechanism of glucose catalysis in different channels is feasible, and also beneficial to improving the catalytic ability and efficiency for sensors. However, by now less attention has been paid on exploring reaction channels of Ni cations in different valence states or its related mechanism on glucose detection.[10,17,46]

In this work, we synthesized laminar-structured Ni-MOF and employed sonication to longitudinally expand Ni-MOF layers for more exposing Ni active sites. It is discovered that the more exposed Ni active sites from the sonication-induced longitudinal expansion of Ni-MOF layers not only contribute to glucose detection efficiency, but also show the oxidation peak evolution of Ni ions with different sonication time, revealing the mechanism of different glucose detection channels. With suitable sonication time, the oxidation of nickel element to Ni(IV) during the formation process has been significantly enhanced, where the Ni(IV) reacts with glucose through the enhanced Ni(IV)/Ni(III) or Ni(IV)/Ni(II) catalysis channels, improving the glucose catalytic current density and linear stability within a broad glucose concentration. More importantly, an all-solid-state, non-enzymatic, non-invasive, and safety level sweat glucose biosensor was developed for household usage, using a solid-state PVA/NaOH electrolyte, which avoids the unsafe and non-convenient severe alkaline liquids or the dilution of sweat,[47,48] and benefits the practicality and commercialization for future non-invasive biosensors.

2. Experimental

2.1 Synthesis of Ni-MOFs

The bulk Ni-MOF was synthesized through a hydrothermal process. First, 0.498 g terephthalic acid (TPA, CAS: 100-21-0, Sigma-Aldrich) and 0.288 g $Ni(NO_3)_2{\cdot}6H_2O$ (CAS: 13478-00-7, Sinopharm Chemical Reagent) were dissolved in 60 mL N,N-dimethylformamide (DMF, CAS: 68-12-2, Sinopharm Chemical

View Article Online
DOI: 10.1039/D0TB01675H

Reagent) under stirring at room temperature to form an emerald transparent solution. Second, 6 mL of 0.4 M NaOH (CAS: 1310-73-2, Sinopharm Chemical Reagent) solution was added in the above emerald transparent solution drop by drop, in accompany with the formation of white flocculent precipitation. Third, the mixture was transferred into a 100 mL Teflon-lined stainless steel autoclave, and kept at 100 °C for 8 hours. The bulk Ni-MOF was obtained by collecting the green powder after the mixture was centrifuged at 4000 rpm, rinsed with DMF three times, and dried at 60 °C.

The Ni-MOF was further treated by ultrasonic method.[38] 30 mg of the obtained bulk Ni-MOF was dispersed in 25 mL alcohol, and ultrasonicated for 0, 30, 60, and 120 min, followed by centrifugation and drying, which were labeled as 0 min Ni-MOF, 30 min Ni-MOF, 60 min Ni-MOF, and 120 min Ni-MOF, respectively

2.2 Glucose Detection Test of Ni-MOFs in Alkaline Solution

The electrochemical performance of Ni-MOF was investigated in 0.1 M NaOH solution with different glucose concentrations using a three-electrode system. The CV, chronoamperometry, electrochemical impedance spectroscopy (EIS), and cycling stability were tested by an Autolab PGSTAT 302N electrochemical workstation. An Ag/AgCl electrode with salt bridge and a metal platinum were used as reference and counter electrodes, respectively. 10 mg Ni-MOFs, 900 µL ethanol, 100 µL water, and 10 µL 5% nafion was mixed uniformly. A glassy carbon electrode (GCE, Φ = 3 mm) casted with 5 µL mixture and dried at 60 °C for 1 hour was used as the working electrode. Dynamic tests in solutions with presence of glucose were conducted under magnetically-stirred mode at 40 rpm, to obtain a stable catalytic current response.

2.3 Preparation of All-Solid-State Sweat Glucose Biosensor

The all-solid-state sweat glucose biosensor consists of working electrode, counter electrode, reference electrode, and polyvinyl alcohol (PVA)/NaOH solid-state electrolytic. 5 µL slurry mixture solution composed of 60 min Ni-MOF, carbon black, and polyvinylidene fluoride (PVDF) with the mass ratio of 8:1:1 was casted on a carbon fiber paper (TORAY), to form a disposable working electrode with an active area of 1 cm × 1 cm. A graphite paper (Crystal Dragon Carbon Technology, Beijing) was employed as the counter electrode. An Ag/AgCl film prepared by immersing an Ag film in a 0.05 M $FeCl_3$ solution for 1 min was served as the reference electrode.[49] The Ag coating was fabricated on polyimide film by a silver mirror reaction.[50] For the solid-state electrolyte, the PVA/NaOH was synthesized by dissolving 2 g PVA (M_w = 1750±50) in 20 mL water, and then dropping 10 mL of 0.3 M NaOH solution, followed by repeatedly freezing and thawing the alkaline mixture until it was solidified into the solid-state electrolyte.[51]

2.4 Stability and Interference of Glucose Detection Test using Disposable Electrode in Alkaline Solution

The disposable working electrode was firstly tested in a three-electrode mode under alkaline conditions for studying its stability and interference performance. To investigate the stability, CV tests and chronoamperometry were employed. For CV tests, the current intensities of oxidation peak at 20 mV s^{-1} were measured in 0.1 M NaOH solution with and without 100 µM glucose every 3 days at room temperature. For chronoamperometry, the current at a constant voltage of 0.55 V in 0.1 M NaOH solution with 100 µM glucose was applied for 6 hours. Interference experiment on the working electrode of disposable biosensor was conducted by dropping 100 µM glucose, 100 mM NaCl, 50 µM dopamine, 50 µM uric acid, and 200 µM urea into an initial 0.1 M NaOH solution and the amperometric response was recorded at a constant voltage of 0.55 V.

2.5 Glucose Detection Test of All-Solid State Sweat Glucose Biosensor

The glucose detection performance of all-solid-state sweat glucose biosensor was systematically investigated using neutral glucose solutions, simulated sweat solutions, and collected sweat solutions, respectively. The glucose detection in neutral glucose solutions, simulated sweat solutions and collected sweat solutions was investigated using all-solid-state sweat glucose biosensor, by dipping neutral glucose solutions and simulated sweat solutions onto the disposable working electrode with different concentrations from 0 to 1600 µM for a few seconds before electrochemical measurements as well as onto a sweating person's forehead for a few seconds who just did a 15-min exercise, respectively. The neutral glucose solutions were synthesized by dissolving glucose powders with different masses of 0 g L^{-1}, 9.91×10^{-3} g L^{-1}, 1.98×10^{-2} g L^{-1}, 3.96×10^{-2} g L^{-1}, 7.93×10^{-2} g L^{-1}, 1.59×10^{-1} g L^{-1}, and 3.17×10^{-1} g L^{-1} in DI water, and the simulated sweat solutions were synthesized by dissolving corresponding masses of glucose powders, 1.55 g L^{-1} NaCl, 4.55×10^{-1} g L^{-1} KCl, 5.83×10^{-2} g L^{-1} Na_2SO_4, 6.01×10^{-1} g L^{-1} urea, and 9.92×10^{-3} g L^{-1} uric acid in DI water.[4]

2.6 Characterizations

The crystallographic patterns were examined by a rotating anode X-ray powder diffractometer (XRD, 18KW/D/max2550VB/PC). A field-emission scanning electron microscope (FESEM, FEI NOVA Nano SEM450) and a transmission electron microscope (TEM, JEM-2100) were used to detect the surface morphology and structure of the Ni-MOFs. The surface chemistry was characterized by a Thermal Scientific ESCALAB 250Xi X-ray photoelectron spectroscope (XPS) with Al anode excited X-ray (Al$K\alpha$ ~ 0.83 nm). The peak shift of the binding energy was corrected by the C 1s peak (284.8 eV)

3. Results and discussion

3.1 Characterization of Ni-MOFs

Fig. 1a shows the crystal structures of Ni-MOFs sonicated for different time (0, 30, 60, and 120 min), with 1 cm × 1 cm X-ray beam area on the surface of Ni-MOF powders during the XRD measurement. Typical diffraction peaks of Ni-MOFs in Fig. 1a at 2θ = 9.30°, 11.68°, 15.64°, 18.66°, 23.68°, 28.18°, and 29.10° are identified as the planes of (1 0 0), (0 1 0), (1 0 -1), (2 0 0), (0 2 0), (2 -2 0), and (-1 -2 1), respectively, as shown in Fig. 1b.[17,52-55] All these XRD peaks of Ni-MOFs match very well with

View Article Online
DOI: 10.1039/D0TB01657H

their simulated XRD patterns (CCDC 638866, space P-1 group).[56]

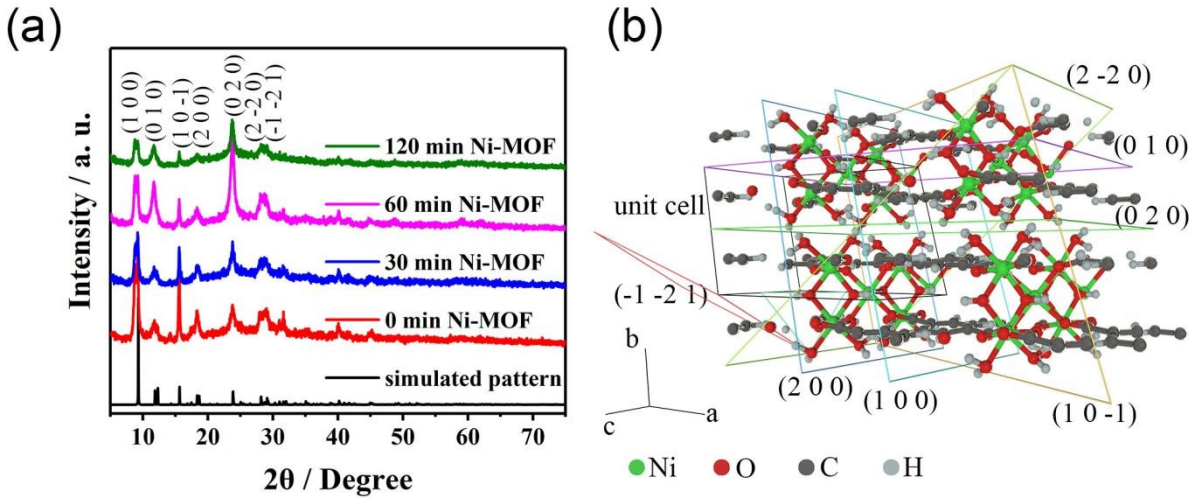

Fig. 1 (a) XRD patterns of Ni-MOFs sonicated for different time of 0, 30, 60, and 120 min. (b) Corresponding crystal planes in Ni-MOF.

The peak-to-baseline intensities of Ni-MOFs with different sonication time derived from Fig. 1a are listed in Table 1. It can be observed that the intensities of (1 0 0), (2 0 0), and (1 0 -1) planes decrease, while the intensities of (0 1 0) and (0 2 0) planes increase with increasing sonication time, because the Ni-MOFs expand along the "b" axis direction after ultrasonic treatment as shown in Fig. 1b, and thus more ordered (0 1 0) and (0 2 0) planes are exposed, while (1 0 0), (2 0 0), and (1 0 -1) planes crush.[52] The intensities of (0 1 0) and (0 2 0) planes increase with the increase of sonication time from 0 to 60 min but further decrease at 120 min, due to the fact that extended sonication causes complete smashes and disorders to these exfoliated planes.

Table 1 Peak-to-baseline intensities of representative crystal faces of Ni-MOFs.

Sample	Peak-to-baseline intensities of representative crystal faces						
	(100)	(010)	(10-1)	(200)	(020)	(2-20)	(-1-21)
0 min Ni-MOF	5.61	1.74	4.79	2.28	2.59	2.20	2.40
30 min Ni-MOF	3.42	1.49	2.58	1.57	2.90	1.96	2.01
60 min Ni-MOF	3.36	3.00	2.03	1.56	5.64	2.34	2.35
120 min Ni-MOF	1.81	1.48	1.15	1.03	2.87	1.56	1.50

The crystalline size D is estimated according to the Scherrer equation (1), with values shown in Table 2:

$$D = K\lambda/(\beta\cos\theta) \quad (1)$$

where K is the shape factor, λ is the X-ray wavelength, β is the full width at half maximum (FWHM) of the diffraction peak, and θ is the Bragg angle. The crystalline sizes in the (0 2 0) direction are estimated to be 7.69, 16.61, 10.58, 7.60 nm for 0, 30, 60, and 120 min Ni-MOFs, respectively. The average crystalline size in the (0 2 0) direction increases with the ultrasonic time increasing from 0 to 60 min, because the ultrasonic treatment breaks the interlayer hydrogen bonds, expands perpendicularly the (0 2 0) face and thus exposes more (0 2 0) planes. However, the average crystalline size in the (0 2 0) direction further decreases when the ultrasonic time is extended from 60 to 120 min, because excessive ultrasonic treatment causes complete smashes and disorders in 120 min Ni-MOF.

Table 2 Estimated average crystalline size.

Sample	(020) direction / nm
0 min Ni-MOF	7.69
30 min Ni-MOF	16.61
60 min Ni-MOF	10.58
120 min Ni-MOF	7.60

Fig. 2 shows the morphological characteristics of Ni-MOFs with different sonication time. The bulk Ni-MOF without sonication (0 min Ni-MOF) in Fig. 2a exhibits a typical thick-sheet structure (~5 μm in diameter) with smooth and flat surface. As shown in Fig. 2b, some smaller thin layers are observed on top of the 0 min Ni-MOF surface, suggesting that the bulk Ni-MOFs should be assembled closely by stacked layers. With the extension of sonication time, the morphology of Ni-MOFs changes obviously. The Ni-MOFs with sonication time of 30, 60, and 120 min are shown in Fig. 2c-h. As shown in Fig. 2c-f, the 30 and 60 min Ni-MOFs present ordered lamellar structures, which are ascribed to the sonication-induced expansion of the Ni-MOFs from compactly-stacked layers (0 min) into loose layers (30 and 60 min) in the longitudinal direction. However, an extended sonication of 120 min causes a complete exfoliation of the Ni-MOFs, with a disordered

structure of exfoliated layers, as displayed in Fig. 2g and h. Meanwhile, the 30, 60, and 120 min Ni-MOFs exhibit smaller sheet with sizes of ~ 2 μm compared with 0 min Ni-MOF (~ 5 μm), because the sonication-induced longitudinal expansion/exfoliation tears up MOF layers in the lateral direction.

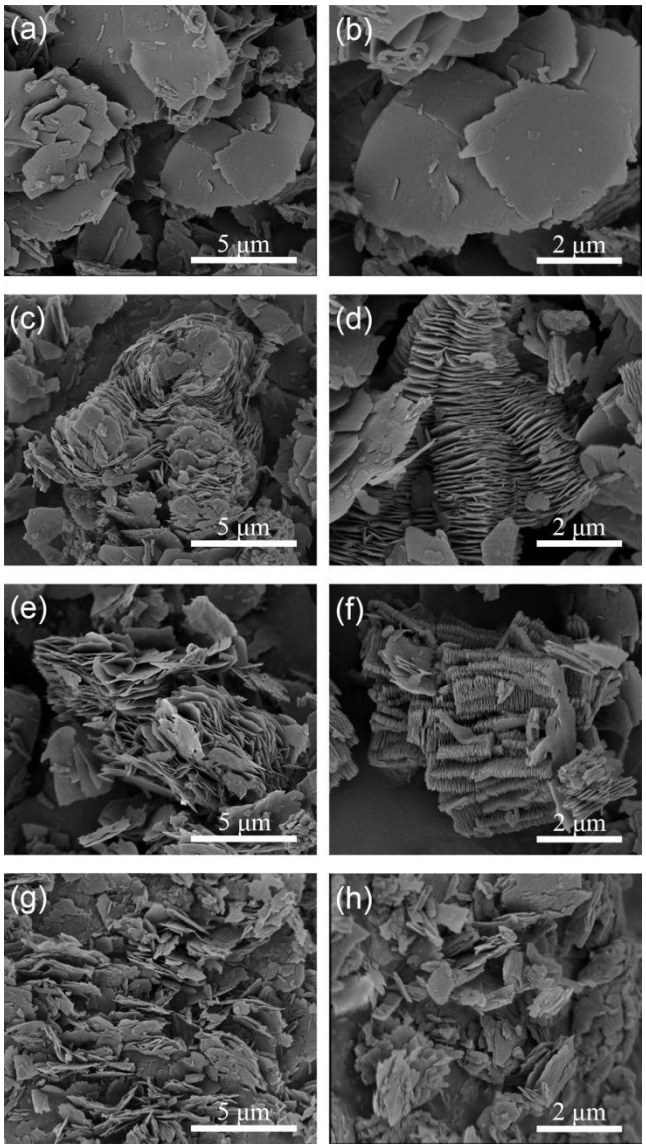

Fig. 2 Low-magnification and high-magnification SEM images of (a, b) 0 min Ni-MOF, (c, d) 30 min Ni-MOF, (e, f) 60 min Ni-MOF and (g, h) 120 min Ni-MOF.

TEM test was performed to investigate the structural details of Ni-MOFs in nanoscale. To prepare TEM samples, all Ni-MOFs powders were dispersed in ethanol and sonicated for 1 min, before being dropped onto the copper grids. All samples sonicated for TEM test exhibit similar exfoliated layers, as shown in Fig. 3a-i. The low-resolution TEM images of Ni-MOFs in Fig. 3a, b, d, e, g, and h reveal uneven color-stratified layer structure, which implies layer stacking. The high-resolution TEM images of Ni-MOFs in Fig. 3c, f, and i show that the spacing of lattice fringe is about ~ 0.20 nm, which matches well with (3 -2 2) plane for Ni-MOF.[53,57] It should be noted that some smaller fragmented Ni-MOF layers with less than 200 nm in diameter are observed in low-resolution TEM image of 120 min Ni-MOF in Fig. 3g which is ascribed to the complete exfoliation and smash of Ni-MOF layers after the extended sonication treatment.

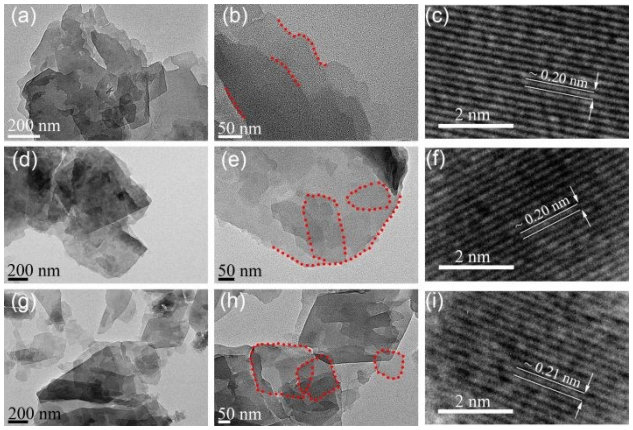

Fig. 3 Low-resolution and high-resolution TEM images of (a-c) 0 min Ni-MOF, (d-f) 60 min Ni-MOF and (g-i) 120 min Ni-MOF.

Fig. 4 shows the surface element valence states of Ni-MOFs with 0, 60, and 120 min sonication treatment. They exhibit similar XPS survey spectra, indicating that the ultrasonic treatment does not change the element bonding structures. The major elements in Ni-MOFs are Ni, O, and C, as shown in their XPS survey spectra in Fig. 4a. The peaks at 855.9 and 873.5 eV in the high-resolution Ni 2p spectrum in Fig. 4b indicate the existence of Ni(II) and are assigned to Ni $2p_{3/2}$ and Ni $2p_{1/2}$, respectively.[17,32,58] The peaks at 531.3 and 532.8 eV in the high-resolution O 1s spectrum in Fig. 4c are attributed to the Ni-O bonds and the adsorbed H_2O molecules, respectively.[17,46] The peaks at 288.3, 285.1, and 284.4 eV in the high-resolution C 1s spectrum in Fig. 4d are attributed to C=O, C-OH, and C-C for the organic ligands, respectively.[53]

View Article Online
DOI: 10.1039/D0TB01657H

Journal Name

ARTICLE

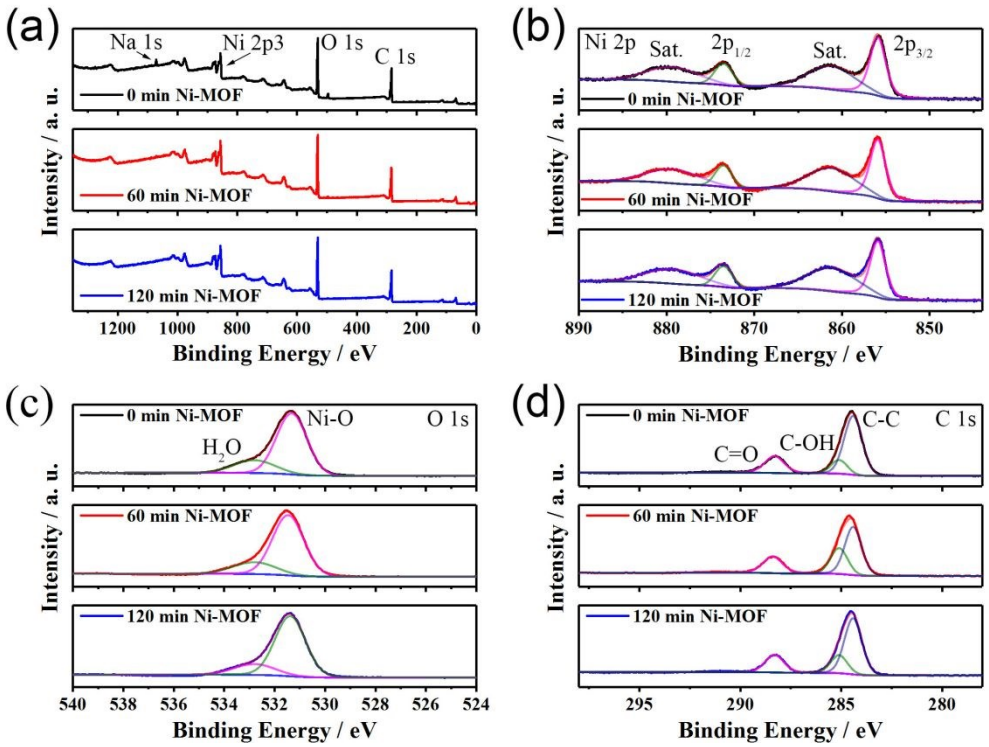

Fig. 4 (a) XPS spectra of Ni-MOFs with different sonication time. High-resolution (b) Ni 2p, (c) O 1s, and (d) C 1s XPS spectra.

Table 3 shows the relative atomic concentrations of Ni-MOFs derived from their survey XPS spectra in Fig. 4a. The atomic concentrations of Ni, O, and C in 0, 60, and 120 min Ni-MOFs are similar, indicating that the sonication does not affect elemental distributions. The weak Na 1s peak at ~ 1071 eV of 0 min Ni-MOF is introduced by NaOH during synthesis, and may exist as interlayer cations.[59,60] This speculation is partly confirmed by the gradually decreasing Na 1s concentrations with increasing sonication time from 1.80 (0 min Ni-MOF), 0.61 (60 min Ni-MOF), to 0.00 (120 min Ni-MOF) at% in Table 3, because the Na cations on the interlayer surfaces are exposed during the sonication-induced expansion and dissolve in solvent.

Table 3 Relative atomic concentrations of Ni-MOFs with different sonication time.

Samples	Relative Atomic Concentrations / at%			
	Ni 2p	O 1s	C 1s	Na 1s
0 min Ni-MOF	4.23	38.19	55.77	1.80
60 min Ni-MOF	5.50	40.29	53.59	0.61
120 min Ni-MOF	5.32	40.94	53.73	0.00

The target Ni-MOF synthesized in this work is referred to as $[Ni_3(OH)_2(C_8H_4O_4)_2\cdot(H_2O)_4]\cdot 2H_2O$.[38,52,56] The XRD diffraction peak positions of all samples match the previous simulation results of the target MOF well,[17,33,52,53,57,61] revealing a spatial framework structure of center Ni^{2+} bonded with TPA ligands.[53] The high-resolution O1s and C 1s XPS spectra in Fig. 4c and d confirm the presence of organic ligands and adsorbed water molecules in all samples. The nickel-oxygen bond at 531.3 eV in O 1s spectrum and the existence of Ni(II) in Ni 2p spectrum indicate the chemical bonding and valence state of nickel element. The results indicate that the target Ni-MOF $[Ni_3(OH)_2(C_8H_4O_4)_2\cdot(H_2O)_4]\cdot 2H_2O$ has been successfully synthesized.

In this work, systematical sonication treatments were conducted on the Ni-MOFs with different sonication time from 0 to 120 min. The evolution of longitudinal expansion (along "b" axis in Fig. 1b) between Ni-MOF interlayers was detected by XRD patterns using 1 cm × 1 cm X-ray beam (Fig. 1a), and observed from SEM images in micrometer scale (Fig. 2). The

View Article Online
DOI: 10.1039/D0TB01657H

XRD peaks of all Ni-MOFs contain crystal planes of (0 1 0), (0 2 0) parallel and (1 0 0), (2 0 0), (1 0 -1) perpendicular to interlayers (plane of "a" and "c" axes in Fig. 1b). The bulk Ni-MOF (0 min Ni-MOF) displays compactly-stacked (0 1 0) and (0 2 0) planes with hydrogen-bond dominant Van der Waals force, as shown in the crystal structure in Fig. 1b and SEM images in Fig. 2a, b.[56] Sonication helps to enhance the longitudinal expansion along "b" axis and break the weak hydrogen bonds, resulting in more exposed (0 1 0) and (0 2 0) planes, which is demonstrated by their enhanced XRD intensities in Fig. 1a. However, an extended sonication of 120 min causes the complete exfoliation of these planes and leads to smash and disorder, which results in the decreased XRD intensities of (0 1 0) and (0 2 0) planes as shown in Fig. 1a. Simultaneously, the sonication-induced longitudinal expansion or even exfoliation along "b" axis crushes the (1 0 0), (2 0 0), and (1 0 -1) planes, resulting in the decreased intensities of their XRD peaks.

3.2 Electrochemical Activation Process of Ni-MOFs and Double-Channel Redox Mechanism

Electrochemical activation process is a common procedure for MOF-based materials.[42,62] During this process, Ni-MOFs were activated and stabilized for 30 cycles by CV at 20 mV s^{-1} in a 0.1 M NaOH solution. The 30 CV cycles of 0, 60, and 120 min Ni-MOFs and their selected CV curves are shown in Fig. 5. Different oxidation potentials for Ni cations have been observed for 0, 60, and 120 min Ni-MOFs during their formation, which is ascribed to the combination of two major oxidation potentials at ~0.44 and ~0.53 V, as shown in Fig. 5 b, e and h. Specially, during the formation of 60 min Ni-MOF in Fig. 5e, the 5th-cycle CV curve shows a distinct small peak at ~0.43 V, indicating the oxidation of Ni(II) to Ni(III),[42] while the 10th-cycle CV curve displays a second prominent oxidation peak at ~0.53 V, indicating a further oxidation of Ni cations into Ni(III) and Ni(IV).[42] Compared with 60 min Ni-MOF, 0 min Ni-MOF exhibits higher oxidation potential at 0.53 V during the formation process, as shown in Fig. 5b, while the lower oxidation potential at 0.44 V dominates during the formation of in 120 min Ni-MOF, as shown in Fig. 5h. The detailed oxidation peak separation in the 30th-cycle CV curves of 0, 60, and 120 min Ni-MOFs by two oxidation potentials of ~0.44 (Ni(II)/Ni(III)) and ~0.53 V (Ni(III)/Ni(IV)) is shown in Fig. 5c, f and i. The amounts of transferred charges ($Q = \int I/\upsilon \, dV$, where Q is total transferred charges in mC cm^{-2}, I is current density in mA cm^{-2}, V is potential in V, and υ is scan rate in mV s^{-1}) at the lower oxidation potential for 60 and 120 min Ni-MOFs are roughly the same, with $Q_{Ni(II)/(III)}$ values of 7.56 and 5.75 mC cm^{-2}, and 0 min Ni-MOF exhibits a smaller $Q_{Ni(II)/(III)}$ value of 2.53 mC cm^{-2}. The Q values at the higher oxidation potential for these Ni-MOFs show significant difference, with $Q_{Ni(III)/(IV)}$ values of 6.73, 15.92, and 2.23 mC cm^{-2} for 0, 60, and 120 min Ni-MOFs, indicating more Ni ions with higher oxidation state present in 60 min Ni-MOF than in 0 and 120 min Ni-MOFs. Correspondingly, the lower oxidation-state Ni cations initially contribute similar low current density values to ~2.5-3 mA cm^{-2} for all Ni-MOFs, and the higher oxidation state Ni cations subsequently contribute different current density values of ~5, ~6, and ~1 mA cm^{-2} for 0, 60, and 120 min Ni-MOFs. Therefore, the higher current density is contributed by the higher-oxidation state Ni cation in this study. In consequence, the 60 min sonication treatment benefits both oxidation modes at lower and higher oxidation potentials, leading to the broadest oxidation area and highest current intensity, as shown in Fig. 5f.

From the CV cycles in Fig. 5 and XRD results in Fig. 1a, we observe that the oxidation state conversion of Ni-MOFs is dependent on their crystallinities. The Ni(III)/Ni(IV) conversion dominates in the formation processes of the well-ordered plane crystals of 0 and 60 min Ni-MOFs. The $Q_{Ni(III)/Ni(IV)}$ value almost doubles in 60 min MOF compared to 0 min MOF, indicating the more exposed surfaces offering more Ni cation active sites for the higher-state conversion. In contrast, the 120 min MOF shows a severe suppression in Ni(III)/Ni(IV) conversion, where the lower oxidation state conversion Ni(II)/Ni(III) dominates in the formation process of the less-ordered plane crystal, where the plane crystal has been destroyed by the excessive sonication treatment.

View Article Online
DOI: 10.1039/D0TB01657H

Journal Name

ARTICLE

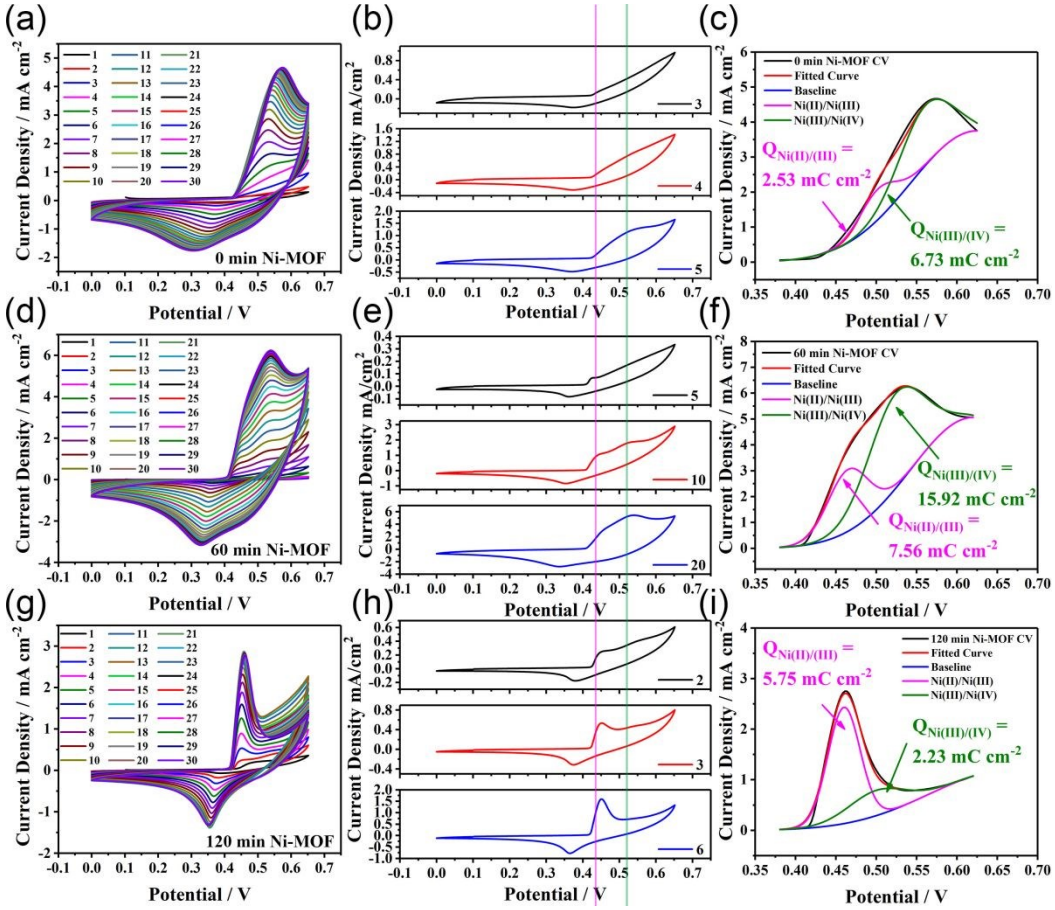

Fig. 5 (a) 30-cycle CV formation process, (b) selected CV cycles, (c) and oxidation peak separation at the 30th CV cycle for 0 min Ni-MOF. (d) 30-cycle CV formation process, (e) selected CV cycles, (f) and oxidation peak separation at the 30th CV cycle for 60 min Ni-MOF. (g) 30-cycle CV formation process, (h) selected CV cycles, (i) and oxidation peak separation at the 30th CV cycle for 120 min Ni-MOF.

During the 30-cycle formation process of Ni-MOF in 0.1 M NaOH, the active Ni component in Ni-MOF turns into $Ni(OH)_2$/NiOOH redox couple,[10] where the NiO_4 bond in Ni-MOF (Fig. 1b) first reacts with OH^- to form -$Ni(OH)_2$ and then is oxidized to -NiOOH unit via a one electron process,[33] as expressed in equations (2) and (3).[63]

$$\beta\text{-Ni(II)(OH)}_2 + OH^- \rightleftharpoons \beta\text{-Ni(III)OOH} + H_2O + e^- \quad (2)$$

$$\alpha\text{-Ni(II)(OH)}_2 + xOH^- \rightleftharpoons \gamma\text{-Ni(IV)OOH} + H_2O + xe^- \quad (3)$$

$$\beta\text{-Ni(III)OOH} \rightleftharpoons \gamma\text{-Ni(IV)OOH} + xe^- \quad (4)$$

where the average oxidation state of γ-phase nickel is 3.5 or higher in equation (3).[64,65] In details, the conversion between β-phase $Ni(OH)_2$ and β-phase NiOOH contributes to the first redox couple Ni(II)/Ni(III) (β(II)/β(III)) as shown in equation (2), while the conversion between α-phase $Ni(OH)_2$ and γ-phase NiOOH is responsible for the second redox couple α(II)/γ(IV) as shown in equation (3).[42] For continuous CV process, γ(IV) is transferred from β(III) via a consecutive one-electron transfer process to form a Ni(III)/Ni(IV) (β(III)/γ(IV)) channel as shown in equation (4).[45] This consecutive evolution of Ni(II)/Ni(III)/Ni(IV) has been confirmed from our observation in the 30-cycle formation process of 60 min MOF as shown in Fig. 5e, where the Ni(II)/Ni(III) peak first emerges at the 5th CV cycle and the Ni(III)/Ni(IV) peak subsequently emerges at the 10th CV cycle. As the Ni(II)/Ni(III) redox couple reaction in equation (2) involves an equivalent proton lattice diffusion, which happens in all Ni-MOF samples, with similar $Q_{Ni(II)/Ni(III)}$ values of 2.53, 7.56, and 5.75 mC cm^{-2} for 0, 60, and 120 min Ni-MOFs.[65,66] The Ni(III)/Ni(IV) redox couple dominates in 0 and 60 min Ni-MOF samples, where the formation of γ-NiOOH requires the insertion of ion and water molecule in ordered interlayers, and sonication-induced interlayer expansion and peeling helps to enhance the insertion process, with $Q_{Ni(III)/(IV)}$ values of 6.73

View Article Online
DOI: 10.1039/D0TB01657H

and 15.92 mC cm^{-2} for 0 and 60 min Ni-MOFs.[65] However, this conversion process based on Ni(III)/Ni(IV) redox couple is fully suppressed in 120 min Ni-MOF sample with a small $Q_{Ni(III)/(IV)}$ value of 2.23 mC cm^{-2}, which is related to its extended sonication-induced smashes and disorders. 60 min Ni-MOF sample exhibits more smaller pieces than 0 min Ni-MOF and better-ordered interlayer expansion than 120 min Ni-MOF. Another possible explanation is that, according to XRD results, an excessive sonication treatment leads to cracks in the organic chains and disordered plane structures, which is not conducive to the stable existence of Ni(IV), considering that Camasso et al. synthesized stabled Ni(IV) in organometallic complexes.[41] Therefore in 60 min Ni-MOF, both Ni(II)/Ni(III) and Ni(III)/Ni(IV) redox couple reactions are prominent, for the ultrasonic treatment makes the active sites fully exposed and improves the chemical dynamic process, as shown in Fig. 5d-f, which leads to its broadest double oxidation CV channels and highest current density, with significant enhancement in Ni(II)/Ni(III) and Ni(III)/Ni(IV) couples compared to 0 min-Ni-MOF, as shown in Fig. 5c and f.

3.3 Double-Channel Glucose Detection Performance of Ni-MOFs in Alkaline Solution

The current response with and without 100 μM glucose as a function of scan rate is shown in Fig. S1, where the electrochemical process and the dependence of current density on scan rate according to the b value are discussed in Supporting Information S1.[67,68] The slopes of log(scan rate) versus log (current density) with and without glucose are different in Fig. S1c, f and i, where the two linear fitting lines intersects at a certain high scan rate between 60 and 100 mV s^{-1}, which means that a current gain can be obtained at lower sweep speeds (< ~ 60 mV s^{-1}) while a current loss can be caused at higher sweep speeds in glucose solution, different with those in non-glucose solution. For this reason, we choose the potential scan rate of 20 mV s^{-1} in the following CV test. The double channel non-enzymatic catalysis of glucose in alkaline condition can be described as equations (2) to (6).[32] One glucose catalysis channel refers to the oxidation of a Ni(II) to a Ni(III) called Ni(II)/Ni(III), and the oxidation of a Ni(III) with a glucose to form a glucolactone and a Ni(II) called Ni(III)/Ni(II). The other glucose catalysis channel refers to the oxidation of a Ni(III) to a Ni(IV) called Ni(III)/Ni(IV), and the reaction of a Ni(IV) with a glucose to form a glucolactone and a Ni(III) called Ni(IV)/Ni(III).

$$Ni(IV) + OH^- + Glucose \rightarrow Ni(III) + Glucolactone + H_2O + e^- \quad (5)$$

$$Ni(III) + OH^- + Glucose \rightarrow Ni(II) + Glucolactone + H_2O + e^- \quad (6)$$

The CV curves of Ni-MOFs in 0.1 M NaOH solution with different glucose concentrations are shown in Fig. 6, where the current density at oxidation peak increases with increasing glucose concentration for all Ni-MOFs. The oxidation peak potential of 0 min Ni-MOF shifts significantly toward higher potentials with increasing glucose concentration, reaching ~0.7 V at 500 and 600 μM. This strong polarization phenomenon indicates that the ion transport is severely hindered at high glucose concentration for 0 min Ni-MOF.[42] The corresponding CV peak current density at oxidation peak exhibits a significant deflection at ~200 μM as shown in Fig. 6b, indicating that 0 min Ni-MOF has a narrow linear response to glucose concentration. The CV peak separation of Ni-MOFs with and without 100 μM glucose by two potentials of ~0.44 and ~0.53 V is shown in Fig. 6 and Fig. S2, respectively.

From the peak separation of CV curves of 0 min Ni-MOF with and without 100 μM glucose in Fig. 6c, the total charge of Q100μM Ni(II)/(III) = 3.47 mC cm^{-2} and Q100μM Ni(III)/(IV) = 8.98 mC cm^{-2} indicate that the glucose catalysis by 0 min Ni-MOF is single Ni(IV)/Ni(III) channel dominant as shown equation (5), while the Ni(III)/Ni(II) channel is suppressed due to the poor kinetics implied by severe polarization.[42] The polarization in oxidation peak potential is alleviated in Ni-MOFs with longer sonication time of 30 and 60 min, where the potential deviations are less than 0.1 V upon changing glucose concentration from 0 to 1000 μM, as shown in Fig. 6d and g. Correspondingly, the linearity of current density at oxidation peak potential versus glucose concentration has also been improved in sonicated Ni-MOFs, with the highest current density and best linearity for 60 min Ni-MOF as shown in Fig. 6h, upon changing glucose concentration from 0 to 1000 μM without significant deflection. As shown in Fig. 6i, the total charge of Q100μM Ni(II)/(III) = 6.77 mC cm^{-2} and Q100μM Ni(III)/(IV) = 16.48 mC cm^{-2} indicate that both the double channels of Ni(III)/Ni(II) and Ni(IV)/Ni(III) are involved in the glucose catalysis using 60 min Ni-MOF, and the Ni(IV)/Ni(III) channel plays a dominant role, as shown in equations (5) and (6). From the peak separation of CV curve of 120 min Ni-MOF in Fig. 6l, the total charge of Q100μM Ni(II)/(III) = 6.23 mC cm^{-2} and Q100μM Ni(III)/(IV) = 5.65 mC cm^{-2} indicate that the glucose catalysis by 120 min Ni-MOF is Ni(III)/Ni(II) channel dominant as shown in equation (6), while the Ni(IV)/Ni(III) channel is suppressed compared to 60 min due to the cracks and disorders in the plane crystal structure caused by the excessive sonication.[41,65] Therefore, the 60 min Ni-MOF exhibits significant increase in integrated areas of both Ni(II)/Ni(III) and Ni(III)/Ni(IV) and obviously enhanced double channel catalysis process compared to other Ni-MOFs. The increase in current density and extended linear range of 60 min Ni-MOF should be attributed to the sonication-induced more expanded (0 1 0) and (0 2 0) planes, which provide more nickel active sites Ni(II) to be oxidized to Ni(III) and Ni(IV) as shown in equations (2)-(4), and improves the chemical dynamic process of the double-channel glucose catalysis described by equations (5) and (6), allowing one active Ni(IV) site to catalyze two glucose molecules through two continuous one-electron reactions of Ni(IV)/Ni(III) and Ni(III)/Ni(II). Therefore, the catalytic efficiency and capacity are improved.

View Article Online
DOI: 10.1039/D0TB01657H

Journal Name

ARTICLE

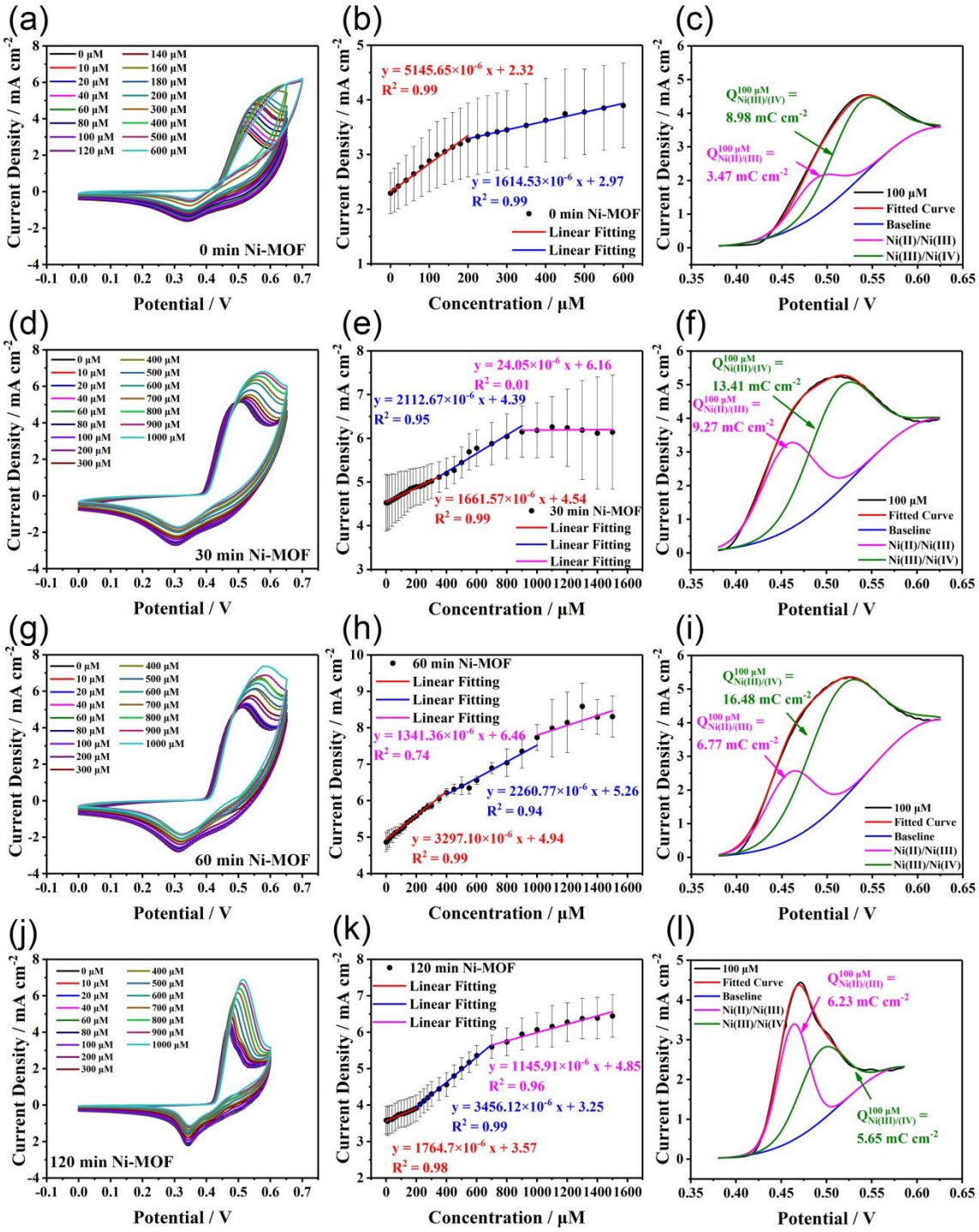

Fig. 6 CV curves at 20 mV s^{-1} in 0.1 M NaOH solutions with different glucose concentrations for (a) 0 min, (d) 30 min, (g) 60 min, and (j) 120 min Ni MOFs. Corresponding current densities at oxidation peaks versus glucose concentrations for (b) 0 min, (e) 30 min, (h) 60 min, and (k)

120 min Ni MOFs. CV peak separations of (c) 0 min, (f) 30 min, (i) 60 min, and (l) 120 min Ni MOFs at 20 mV s^{-1} in 0.1 M NaOH solution with 100 μM glucose.

View Article Online
DOI: 10.1039/D0TB01657H

Fig. 7a shows the real-time current density response of Ni-MOFs to gradually increasing glucose concentration by dropping corresponding volume of 5 mM glucose in 0.1 M NaOH solution, at a constant potential value of 0.55 V. Fig. 7b is the magnified plot of Fig. 7a at first 50 seconds. The lines with noise at the bottom in Fig. 7a and b are real-time experimental data, and the pulsed curves refer to average values derived from 100 real-time data points collected within 10 s. The average current density and deviation values in Fig. 7c-f in 0.1 M NaOH solutions with different glucose concentrations are derived from 100 real-time current data points collected within 10 s at a constant potential value of 0.55 V. At low glucose concentration of less than ~ 700 μM, all Ni-MOFs show similar current responses. The sensitivity is calculated to be 2.62 μA mM^{-1} cm^{-2} for 0 min Ni-MOF ranging from 10 to 1000 μM with a low detection limit of ~1.12 μM (signal-to-noise = 3, S/N = 3), 3.26 μA mM^{-1} cm^{-2} for 30 min Ni-MOF ranging from 10 to 700 μM with a low detection limit of ~0.52 μM (S/N = 3), 3.03 μA mM^{-1} cm^{-2} for 60 min Ni-MOF ranging from 10 to 2000 μM with a low detection limit of ~1.16 μM (S/N = 3), and 2.84 μA mM^{-1} cm^{-2} for 120 min Ni-MOF ranging from 10 to 700 μM with a low detection limit of ~0.25 μM (S/N = 3). With increasing glucose concentration, 60 min Ni-MOF can still maintain the higher current response with good linearity compared with 0, 30, and 120 min Ni-MOFs, as shown in Fig. 7c-f, which is ascribed to the synergistic double-channel catalytic model.

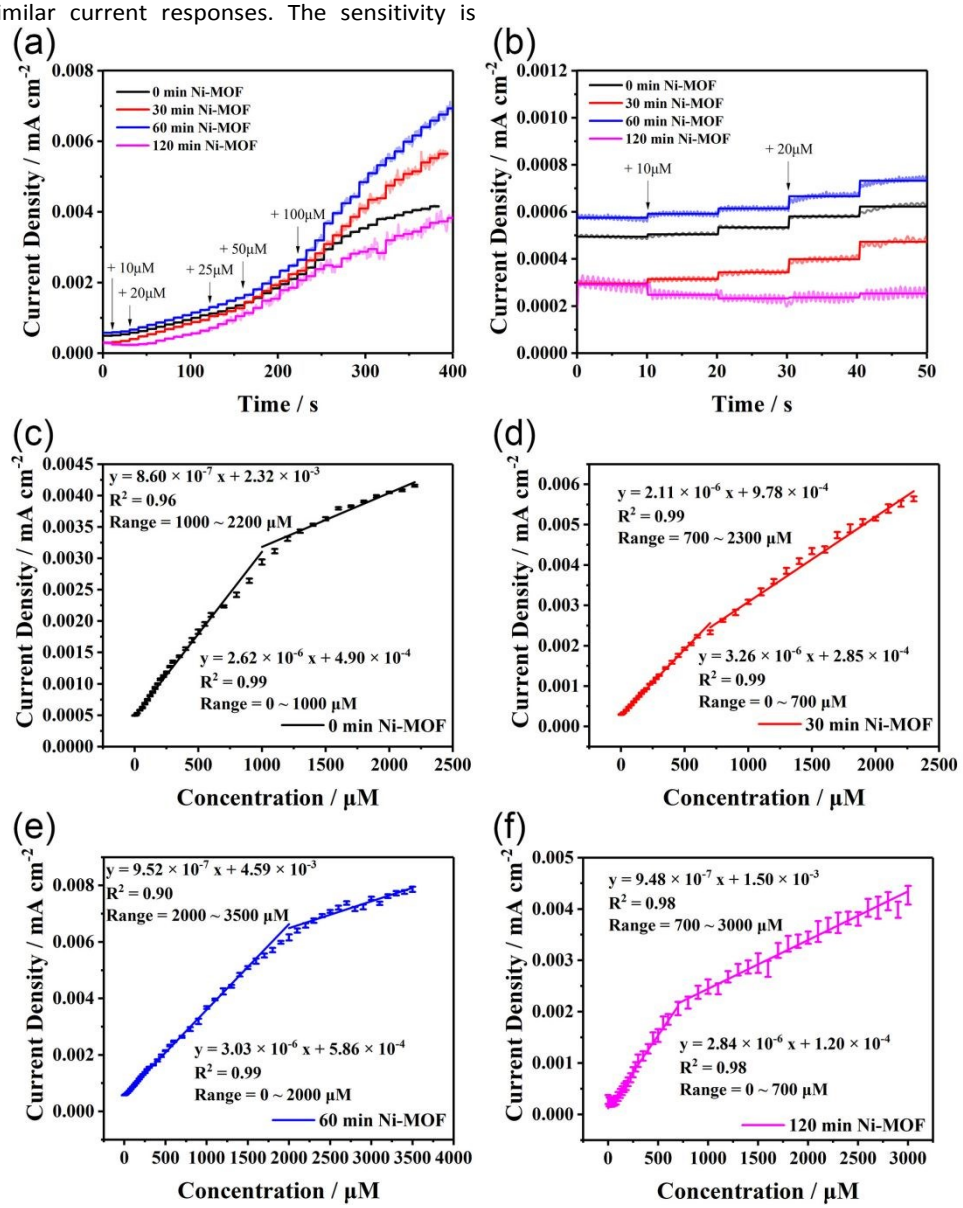

Fig. 7 (a) Amperometric response of Ni-MOFs to glucose at a constant potential value of 0.55 V and (b) magnified plot at first 50 seconds. The pulsed curves represent the average values, and the lines with noise are the real-time experimental data. Corresponding average current density and deviation values versus various glucose concentrations for (c) 0 min, (d) 30 min, (e) 60 min, and (f) 120 min Ni-MOFs.

View Article Online DOI: 10.1039/D0TB01657H

3.4 Glucose Detection Mechanism

To further detect the mechanism of glucose catalysis, a statistic chronoamperogram test (without magnetic stirring) of Ni-MOFs was conducted in 0.1 M NaOH solutions with and without 100 μM glucose as shown in Fig. 8a, where the current data was collected at a constant voltage of 0.55 V and analyzed by Cottrell's equation (7) as shown in Fig. 8b.

$$I_t = n\,F\,A\,D^{1/2}C\,\pi^{-1/2}t^{-1/2} \quad (7)$$

where I_t is chronoamperometry current (A), n is the number of electrons in the redox process of 1, F is the Faraday constant of 96485 C mol^{-1}, A is electrode surface area of 0.07 cm^2, C (mol cm^{-3}) and D (cm^2 s^{-1}) are the bulk concentration of 1.001×10^{-4} mol cm^{-3} (0.1 M + 100 μM) and the diffusion coefficient, respectively.[46,69] The slopes of the fitted linear curves in Fig. 8b are proportional to the diffusion coefficients D. Therefore, for single-electron process, the diffusion coefficients D were calculated to be 8.15×10^{-7}, 1.51×10^{-6} and 1.04×10^{-6} cm^2 s^{-1} for 0, 60, and 120 min Ni-MOFs for catalytic process, respectively. Detailed calculations are shown in Supporting Information S2.

The electrode surface area of 0.07 cm^2 is a fixed value via electrode fabrication. The active surface area related to glucose detection performance of Ni-MOFs was analyzed by Randles-Sevcik equation (8).

$$I_p = 0.4463\,A\,C\,\left(\frac{F^3}{RT}\right)^{1/2} n^{3/2}D^{1/2}\nu^{1/2} \quad (8)$$

where I_p is oxidation peak current (A) from CV curves in Fig. S1a, b, d, e and g, h. n is the number of electrons in the redox process (n = 1) for single electron process, F is the Faraday constant of 96485 C mol^{-1}, R is gas constant of 8.314 J mol^{-1} K^{-1}, T is thermodynamic temperature of 298 K, υ is CV scan rate of 0.02 V s^{-1}, D is the diffusion coefficients derived by Cottrell's equation (equation 6), and A (cm^2) is the active surface area related to glucose detection performance of Ni-MOF electrode.[70,71] Therefore, we can roughly estimate the active surface area related to glucose detection performance of Ni-MOF electrode in 0.1 M NaOH solution with 100 μM glucose to be 0.09, 0.16, and 0.06 cm^2 for 0, 60, and 120 min Ni-MOFs, respectively. Therefore, the increase in diffusion coefficient and electrochemically active surface area demonstrates the improvement in electrochemical performance of layered Ni-MOF by sonication treatment. It is interesting to note that the active surface areas of 0 and 120 min Ni-MOFs (0.09 and 0.06 cm^2) are close to the electrode surface area (0.07 cm^2), while the active surface area of 60 min Ni-MOF (0.16 cm^2) is much larger than the electrode surface area (0.07 cm^2), indicating that sonication-induced longitudinal-expansion has a positive effect on promoting the activity. Detailed calculations are shown in Supporting Information S3.

The current density versus time data in Fig. 8a was analyzed by equation (9) as shown in Fig. 8c.

$$\frac{I_{cat}}{I_L} = \pi^{1/2}(K_{cat}C\,t)^{1/2} \quad (9)$$

where I_{cat} and I_L are the currents in 0.1 M NaOH solutions with and without 100 μM glucose, C (mol cm^{-3}) is the bulk glucose concentration of 10^{-7} mol cm^{-3} (100 μM), and K_{cat} is catalytic rate constant.[46] I_{cat}/I_L and $t^{1/2}$ reveal a linear relationship as shown in Fig. 8c. Therefore, K_{cat} values were calculated to be 2.56×10^4, 2.47×10^5, and 1.09×10^4 cm^3 mol^{-1} s^{-1} for 0, 60, and 120 min Ni-MOFs, respectively. 60 min Ni-MOF exhibits the highest K_{cat} value, indicating its highest catalytic rate.

The EIS results of Ni-MOFs are shown in Fig. 8d, with solid dots representing the results in 0.1 M NaOH solution and hollow dots representing the results in 0.1 M NaOH solution with 100 μM glucose. In general, the semicircle radius in the high-frequency region tends to decrease with increasing sonication time, indicating a decrease in the charge transfer resistance of Ni-MOF electrode, which is ascribed to the fast ionic transport of smaller topographic structures.[65,66] The impedance of all samples increases slightly in the presence of 100 μM glucose, which is ascribed to the glucose-related restricted kinetics process, confirmed by the calculated b values in Fig. S1c, f and i.[72]

View Article Online
DOI: 10.1039/D0TB01657H

Journal Name

ARTICLE

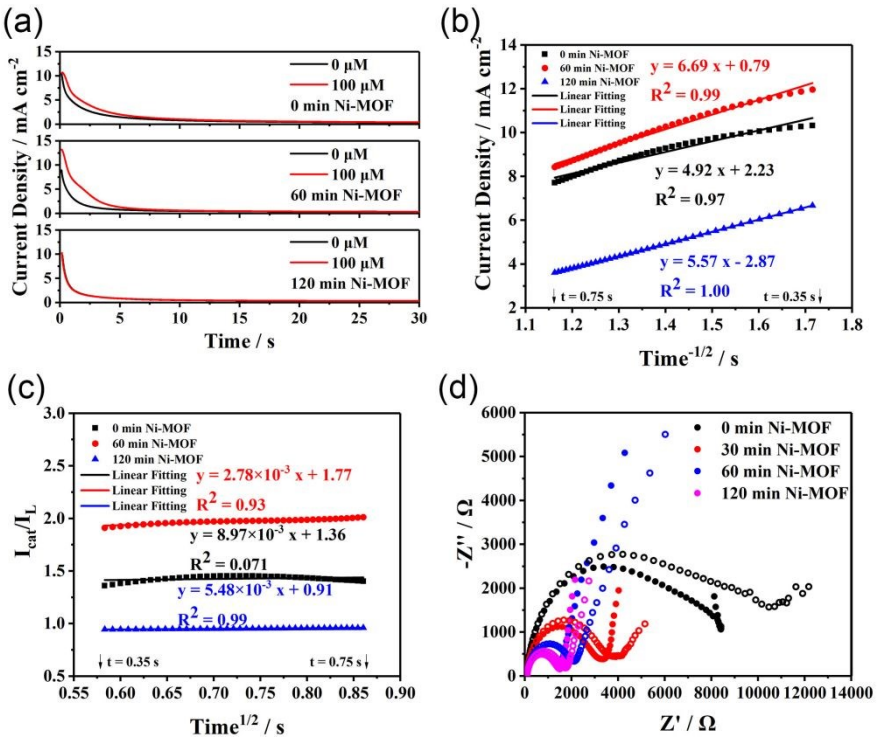

Fig. 8 (a) Chronoamperograms of Ni-MOFs in 0.1 M NaOH solution with 100 μM glucose. (b) Current density versus negative square root of time derived from (a). (c) I_{cat}/I_L versus square root of time derived from (a). (d) EIS results of Ni-MOFs with solid dots representing the results in 0.1 M NaOH solution and hollow dots representing the results in 0.1 M NaOH solution with 100 μM glucose.

3.5 Stability and Interference of Glucose Detection Performance using Disposable Electrode in Alkaline Solution

The long-term stability of the disposable 60 min Ni-MOF working electrode was firstly tested by CV and chronoamperometry as shown in Fig. 9a and b. The current response intensity to glucose tends to decrease with time, because the activity of the Ni-MOF material decreases with the increased CV scan cycles. The average current density versus time shown in Fig. 9b was tested at a constant voltage of 0.55 V for 6 hours in 0.1 M NaOH solution with 100 μM glucose, with each average value is derived from 120 data points. The current maintains 90% of its initial value upon the continuous 6-hour measurement. Interference study on the disposable 60 min Ni-MOF working electrode was conducted by dropping 100 μM glucose, 100 mM NaCl, 50 μM dopamine, 50 μM uric acid, and 200 μM urea into an initial 0.1 M NaOH solution, marked as a, b, c, d and e processes, and the amperometric response was recorded at a constant voltage of 0.55 V, as shown in Fig. 9c. The current density change ratios relative to baseline derived from Fig. 9c were calculated to be 143.9% for 100 μM glucose, 25.1% for 100 mM NaCl, 56.6% for 50 μM dopamine, 10.2% for 50 μM uric acid, and 67.5% for 200 μM urea in an initial 0.1 M NaOH solution, respectively. The disposable 60 min Ni-MOF working electrode shows excellent anti-interference ability to NaCl and uric acid in sweat. The current response to glucose was 5.73, 14.11, 2.13, and 2.54 times higher than those to NaCl, uric acid, urea, and dopamine, respectively. Fig. 9d shows that the current response time for glucose detection using the disposable Ni-MOF electrode during the interference test is less than 3 second. The stability and interference tests show excellent potentials of this disposable 60 min Ni-MOF electrode for a sweat glucose sensor.

View Article Online
DOI: 10.1039/D0TB01657H

Journal Name

ARTICLE

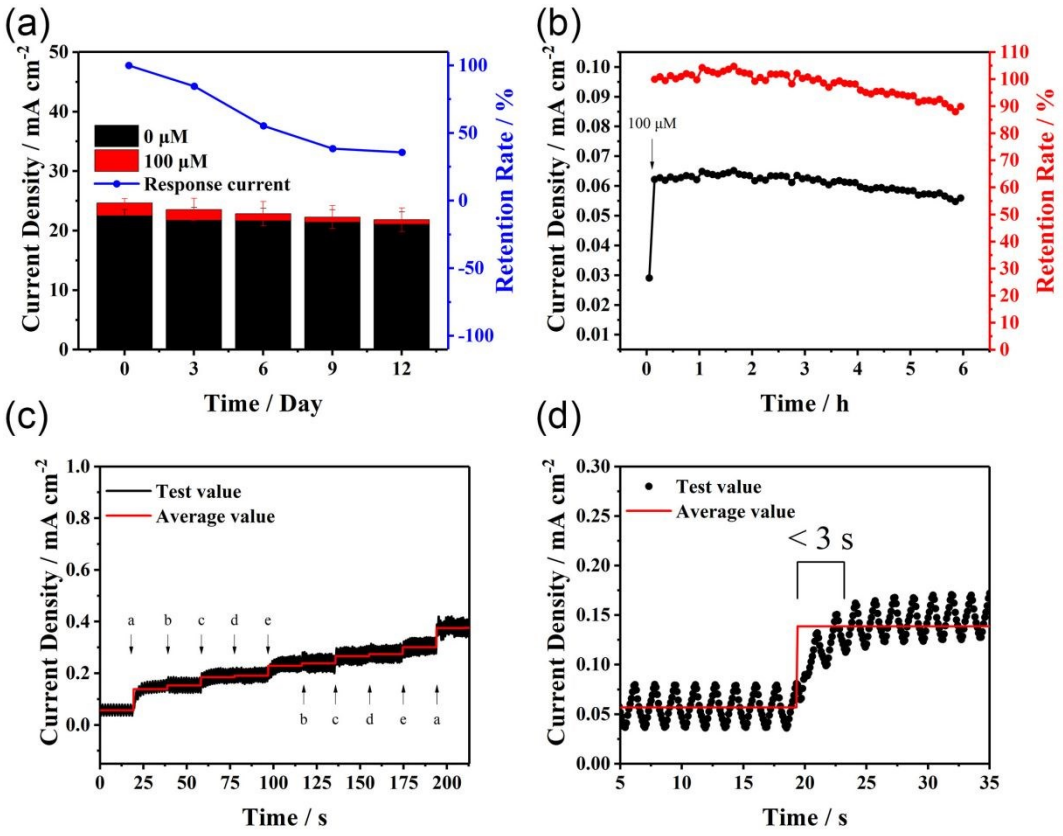

Fig. 9 Long-term stability of the disposable 60 min Ni-MOF electrode, (a) by CV test over a 12-day period at room temperature and (b) by chronoamperograms at a constant voltage of 0.55 V in 100 μM glucose for 6 hours. (c) Interference study of amperometric response at a constant voltage of 0.55 V by dropping 100 μM glucose, 100 mM NaCl, 50 μM dopamine, 50 μM uric acid, and 200 μM urea into an initial 0.1 M NaOH solution, marked as a, b, c, d and e processes. (d) The response time for glucose detection is less than 3 second.

3.6 Design and Performance of All-Solid-State Non-Enzymatic Sweat Glucose Biosensor

As shown in Fig. 10a and b, the all-solid-state non-enzymatic sweat glucose biosensor is composed of a 60 min Ni-MOF based disposable electrode, a solid electrolyte, a working electrode, a counter electrode, and a reference electrode. The disposable electrode soaked with sweat was inserted into the device and contacted with the working electrode. Neutral solutions with different glucose concentrations from 0 to 1600 μM were dropped onto the disposable electrode for CV test at 20 mV s^{-1} as shown in Fig. 10c, with their derived current intensities at different potentials shown in the Fig. 10d. A disposable electrode soaked with the simulated sweat solutions was inserted into the all-solid-state device for a CV test, with their current density values obtained at 0.75 V, as shown in Fig. 10e. By comparing the glucose detection without and with interfering substances at 0.75 V in Fig. 10d and e, it can be found that the sensitivity of the device to detect glucose is basically not affected by interfering substances. An increase in current with presence of interfering substances should come from the highly-conductive salt-containing interfering substances. Sweat solutions were collected from a male adult's forehead after a moderate exercise, and disposable electrodes were soaked with these sweat solutions. The CV measurements were conducted using the all-solid-state device, and the results are shown in Fig. 10f, which display the sweat glucose concentrations of a male adult at different time of a day according to his physiological changes, revealing the promising application of the all-solid-state sweat glucose device for non-invasive enzyme-free monitoring.

View Article Online
DOI: 10.1039/D0TB01657H

Journal Name

ARTICLE

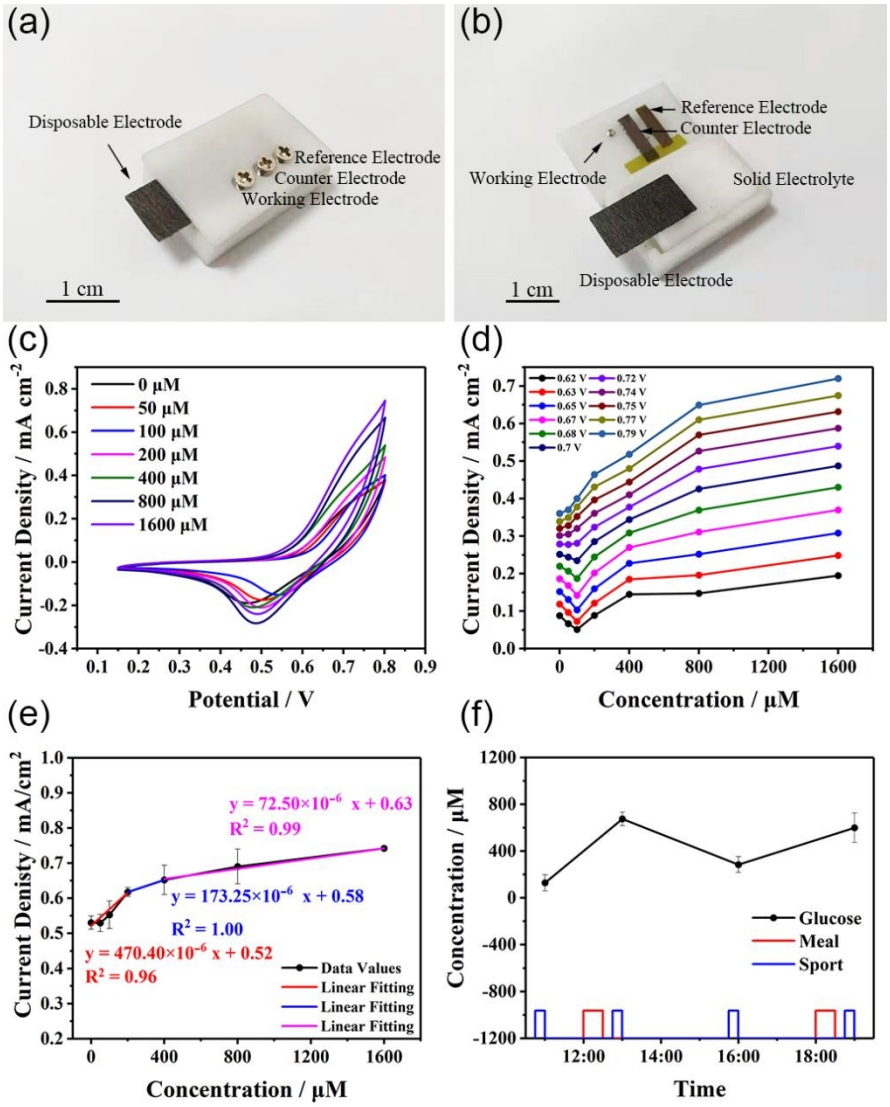

Fig. 10 (a) and (b) Photos of an all-solid-state non-enzymatic sweat glucose biosensor device. (c) CV curves at 20 mV s^{-1} in neutral solutions with different glucose concentrations. (d) Current density versus glucose concentration derived from (c). (e) Current density versus simulated sweat concentration derived from the CV curve at 0.75 V. (f) Glucose detection using collected sweat.

3.7 Comparison of Current Response and Linear Range in Glucose Detection with Other Studies

The comparison of current response and linear range in glucose detection using 60 min Ni-MOF with other studies are shown in Table S1. Compared with the glucose biosensors in previous works, the 60 min Ni-MOF shows a high sensitivity of 3297.10 μA mM^{-1} cm^{-2}, low detection limit of ~8.97 μM (S/N = 3) and wide linear response range from 10 to 400 μM from the CV test as well as a high sensitivity of 3.03 μA mM^{-1} cm^{-2}, low detection limit of ~1.16 μM (S/N = 3) and wide linear response range from 10 to 2000 μM from the chronoamperometry test. The superior glucose detection performance of 60 min Ni-MOF is ascribed to the following reasons: (1) the sonication-induced longitudinal expansion of Ni-MOFs increases the exposed layers and active nickel ion sites; (2) the synergistic Ni(III)/Ni(II) and Ni(IV)/Ni(III) double-channel catalytic model improves the catalytic efficiency and capacity.

4. Conclusions

In this work, we investigated the ultrasonic effects on glucose catalytic performance of Ni-MOFs and explored double-channel catalysis mechanism for glucose detection. The 60 min sonication treated Ni-MOF exhibits more regularly-exposed layers and active nickel ion sites, contributing to enhanced Ni(III)/Ni(II) and more significant Ni(IV)/Ni(III) double nickel cation channels compared to 0 min Ni-MOF. Therefore, the 60 min Ni-MOF shows an expanded glucose current response linear range of 10 ~ 400 μM, high sensitivity of 3297.10 μA mM^{-1} cm^{-2} and low detection limit of ~8.97 μM (S/N = 3) from the CV test as well as an expanded glucose current response linear range of 10 ~ 2000 μM, high sensitivity of 3.03 μA mM^{-1} cm^{-2} and low detection limit of ~1.16 μM (S/N = 3) from the chronoamperometry test. An all-solid-state glucose sensor using a PVA/NaOH solid-sated electrolyte and a disposable 60 min Ni-MOF working electrode was assembled for non-enzymatic sweat glucose detection, showing a sensitivity of 470.40 μA mM^{-1} cm^{-2} from 0 to 200 μM. The strategy in this work should be promisingly applied in exploring high-performance Ni-based sensing materials for safe and facile non-enzymatic sweat glucose detection.

Conflicts of interest

There are no conflicts to declare.

Acknowledgements

This work is sponsored by National Natural Science Foundation of China (61804054), Natural Science Foundation of Shanghai (18ZR1410400), Shanghai Sailing Program (17YF1403300), the Shanghai Aerospace Science and Technology Innovation Fund (SAST2019-067), the Fundamental Research Funds for the Central Universities (222201714017), and the Social Development Program of Shanghai (17DZ1200900, 18DZ2252400).

Notes and references

1. E. V. Karpova, E. V. Shcherbacheva, A. A. Galushin, D. V. Vokhmyanina, E. E. Karyakina and A. A. Karyakin, Noninvasive diabetes monitoring through continuous analysis of sweat using flow-through glucose biosensor, *Anal. Chem.*, 2019, **91**, 3778-3783.
2. V. E. Coyle, A. E. Kandjani, M. R. Field, P. Hartley, M. Chen, Y. M. Sabri and S. K. Bhargava, Co3O4 needles on Au honeycomb as a non-invasive electrochemical biosensor for glucose in saliva, *Biosens. Bioelectron.*, 2019, **141**, 111479.
3. J. Moyer, D. Wilson, I. Finkelshtein, B. Wong and R. Potts, Correlation between sweat glucose and blood glucose in subjects with diabetes, *Diabetes Technol. Ther.*, 2012, **14**, 398-402.
4. C. J. Harvey, R. F. LeBouf and A. B. Stefaniak, Formulation and stability of a novel artificial human sweat under conditions of storage and use, *Toxicol. In Vitro*, 2010, **24**, 1790-1796.
5. Y. Zhao, Q. Zhai, D. Dong, T. An, S. Gong, Q. Shi and W. Cheng, Highly stretchable and strain-insensitive fiber-based wearable electrochemical biosensor to monitor glucose in the sweat, *Anal. Chem.*, 2019, **91**, 6569-6576.
6. X. Zhang, Y. Xu and B. Ye, An efficient electrochemical glucose sensor based on porous nickel-based metal organic framework/carbon nanotubes composite (Ni-MOF/CNTs), *J. Alloys Compd.*, 2018, **767**, 651-656.
7. J. Zhou, M. Min, Y. Liu, J. Tang and W. Tang, Layered assembly of NiMn-layered double hydroxide on graphene oxide for enhanced non-enzymatic sugars and hydrogen peroxide detection, *Sens. Actuators B Chem.*, 2018, **260**, 408-417.
8. H. Xu, C. Xia, S. Wang, F. Han, M. K. Akbari, Z. Hai and S. Zhuiykov, Electrochemical non-enzymatic glucose sensor based on hierarchical 3D Co_3O_4/Ni heterostructure electrode for pushing sensitivity boundary to a new limit, *Sens. Actuators B Chem.*, 2018, **267**, 93-103.
9. M. Xu, D. Obodo and V. K. Yadavalli, The design, fabrication, and applications of flexible biosensing devices, *Biosens. Bioelectron.*, 2019, **124-125**, 96-114.
10. D. W. Hwang, S. Lee, M. Seo and T. D. Chung, Recent advances in electrochemical non-enzymatic glucose sensors - A review, *Anal. Chim. Acta*, 2018, **1033**, 1-34.
11. S. Darvishi, M. Souissi, F. Karimzadeh, M. Kharaziha, R. Sahara and S. Ahadian, Ni nanoparticle-decorated reduced graphene oxide for non-enzymatic glucose sensing: an experimental and modeling study, *Electrochim. Acta*, 2017, **240**, 388-398.
12. H. Nie, Z. Yao, X. Zhou, Z. Yang and S. Huang, Nonenzymatic electrochemical detection of glucose using well-distributed nickel nanoparticles on straight multi-walled carbon nanotubes, *Biosens. Bioelectron.*, 2011, **30**, 28-34.
13. F. J. García-García, P. Salazar, F. Yubero and A. R. González-Elipe, Non-enzymatic glucose electrochemical sensor made of porous NiO thin films prepared by reactive magnetron sputtering at oblique angles, *Electrochim. Acta*, 2016, **201**, 38-44.
14. S. Liu, B. Yu and T. Zhang, A novel non-enzymatic glucose sensor based on NiO hollow spheres, *Electrochim. Acta*, 2013, **102**, 104-107.
15. M. M. Guo, X. L. Yin, C. H. Zhou, Y. Xia, W. Huang and Z. Li, Ultrasensitive nonenzymatic sensing of glucose on Ni(OH)2-coated nanoporous gold film with two pairs of electron mediators, *Electrochim. Acta*, 2014, **142**, 351-358.
16. K. E. Toghill and R. G. Compton, Electrochemical Non-enzymatic Glucose Sensors: A Perspective and an Evaluation, *Int. J. Electrochem. Sci.*, 2010, **5**, 1246-1301.
17. W. Lu and X. Wu, Ni-MOF nanosheet arrays: efficient non-noble-metal electrocatalysts for non-enzymatic monosaccharide sensing, *New J. Chem.*, 2018, **42**, 3180-3183.
18. W. S. Kim, G. J. Lee, J. H. Ryu, K. Park and H. K. Park, A flexible, nonenzymatic glucose biosensor based on Ni-coordinated, vertically aligned carbon nanotube arrays, *RSC Adv.*, 2014, **4**, 48310-48316.

19. Y. T. Liao, V. C. Nguyen, N. Ishiguro, A. P. Young, C. K. Tsung and K. C. W. Wu, Engineering a homogeneous alloy-oxide interface derived from metal-organic frameworks for selective oxidation of 5-hydroxymethylfurfural to 2,5-furandicarboxylic acid, *Appl. Catal. B*, 2020, **270**, 118805.
20. Y. T. Liao, B. M. Matsagar and K. C. W. Wu, Metal–Organic Framework (MOF)-Derived Effective Solid Catalysts for Valorization of Lignocellulosic Biomass, *ACS Sustain. Chem. Eng.*, 2018, **6**, 13628-13643.
21. H. Konnerth, B. M. Matsagar, S. S. Chen, M. H. G. Prechtl, F. K. Shieh and K. C. W. Wu, Metal-organic framework (MOF)-derived catalysts for fine chemical production, *Coord. Chem. Rev.*, 2020, **416**, 213319.
22. C. C. Chueh, C. L. Chen, Y. A. Su, H. Konnerth, Y. J. Gu, C. W. Kung and K. C. W. Wu, Harnessing MOF materials in photovoltaic devices: recent advances, challenges, and perspectives, *J. Mater. Chem. A*, 2019, **7**, 17079-17095.
23. C. C. Lee, C. L. Chen, Y. T. Liao, K. C. W. Wu and C. C. Chueh, Enhancing efficiency and stability of photovoltaic cells by using perovskite/Zr-MOF heterojunction including bilayer and hybrid structures, *Adv. Sci.*, 2019, **6**, 1801715.
24. C. Wang, J. Kim, J. Tang, J. Na, Y. M. Kang, M. Kim, H. Lim, Y. Bando, J. Li and Y. Yamauchi, Large-scale synthesis of MOF-derived superporous carbon aerogels with extraordinary adsorption capacity for organic solvents, *Angew. Chem. Int. Ed.*, 2020, **59**, 2066-2070.
25. J. Tang, R. R. Salunkhe, H. Zhang, V. Malgras, T. Ahamad, S. M. Alshehri, N. Kobayashi, S. Tominaka, Y. Ide, J. H. Kim and Y. Yamauchi, Bimetallic Metal-organic frameworks for controlled catalytic graphitization of nanoporous carbons, *Sci. Rep.*, 2016, **6**, 30295.
26. Y. V. Kaneti, J. Zhang, Y. B. He, Z. Wang, S. Tanaka, M. S. A. Hossain, Z. Z. Pan, B. Xiang, Q. H. Yang and Y. Yamauchi, Fabrication of an MOF-derived heteroatom-doped Co/CoO/carbon hybrid with superior sodium storage performance for sodium-ion batteries, *J. Mater. Chem. A*, 2017, **5**, 15356-15366.
27. C. Wang, J. Kim, J. Tang, M. Kim, H. Lim, V. Malgras, J. You, Q. Xu, J. Li and Y. Yamauchi, New Strategies for Novel MOF-Derived Carbon Materials Based on Nanoarchitectures, *Chem*, 2020, **6**, 19-40.
28. S. Hou, X. Xu, M. Wang, Y. Xu, T. Lu, Y. Yao and L. Pan, Carbon-incorporated Janus-type Ni2P/Ni hollow spheres for high performance hybrid supercapacitors, *J. Mater. Chem. A*, 2017, **5**, 19054-19061.
29. Y. Li, G. Zhu, H. Huang, M. Xu, T. Lu and L. Pan, A N, S dual doping strategy via electrospinning to prepare hierarchically porous carbon polyhedra embedded carbon nanofibers for flexible supercapacitors, *J. Mater. Chem. A*, 2019, **7**, 9040-9050.
30. Y. Li, M. Xie, X. Zhang, Q. Liu, D. Lin, C. Xu, F. Xie and X. Sun, Co-MOF nanosheet array: A high-performance electrochemical sensor for non-enzymatic glucose detection, *Sens. Actuators B Chem.*, 2019, **278**, 126-132.
31. L. Zhang, X. Ma, H. Liang, H. Lin and G. Zhao, A non-enzymatic glucose sensor with enhanced anti-interference ability based on a MIL-53(NiFe) metal-organic framework, *J. Mater. Chem. B*, 2019, **7**, 7006-7013.
32. X. Xiao, S. Zheng, X. Li, G. Zhang, X. Guo, H. Xue and H. Pang, Facile synthesis of ultrathin Ni-MOF nanobelts for high-efficiency determination of glucose in human serum, *J. Mater. Chem. B*, 2017, **5**, 5234-5239.
33. F. Wang, X. Chen, L. Chen, J. Yang and Q. Wang, High-performance non-enzymatic glucose sensor by hierarchical flower-like nickel(II)-based MOF/carbon nanotubes composite, *Mater. Sci. Eng. C Mater. Biol. Appl.*, 2019, **96**, 41-50.
34. C. Zhang, Q. Zhang, K. Zhang, Z. Xiao, Y. Yang and L. Wang, Facile synthesis of a two-dimensional layered Ni-MOF electrode material for high performance supercapacitors, *RSC Adv.*, 2018, **8**, 17747-17753.
35. W. Li, S. Lv, Y. Wang, L. Zhang and X. Cui, Nanoporous gold induced vertically standing 2D NiCo bimetal-organic framework nanosheets for non-enzymatic glucose biosensing, *Sens. Actuators B Chem.*, 2019, **281**, 652-658.
36. M. Li, L. Liu, Y. Xiong, X. Liu, A. Nsabimana, X. Bo and L. Guo, Bimetallic MCo (M= Cu, Fe, Ni, and Mn) nanoparticles doped-carbon nanofibers synthetized by electrospinning for nonenzymatic glucose detection, *Sens. Actuators B Chem.*, 2015, **207**, 614-622.
37. T. S. Munonde, H. Zheng and P. N. Nomngongo, Ultrasonic exfoliation of NiFe LDH/CB nanosheets for enhanced oxygen evolution catalysis, *Ultrason. Sonochem.*, 2019, **59**, 104716.
38. Y. Yan, P. Gu, S. Zheng, M. Zheng, H. Pang and H. Xue, Facile synthesis of an accordion-like Ni-MOF superstructure for high-performance flexible supercapacitors, *J. Mater. Chem. A*, 2016, **4**, 19078-19085.
39. K. T. Lee, Y. C. Liang, H. H. Lin, C. H. Li and S. Y. Lu, Exfoliated SnS_2 nanoplates for enhancing direct electrochemical glucose sensing, *Electrochim. Acta*, 2016, **219**, 241-250.
40. S. Lennon and F. Robinson, The experimental determination of potential-pH diagrams for the Ni-H_2O and low alloy steel-H_2O systems, *Corros. Sci.*, 1986, **26**, 995-1007.
41. N. M. Camasso and M. S. Sanford, Design, synthesis, and carbon-heteroatom coupling reactions of organometallic nickel (IV) complexes, *Science*, 2015, **347**, 1218-1220.
42. M. S. Rahmanifar, H. Hesari, A. Noori, M. Y. Masoomi, A. Morsali and M. F. Mousavi, A dual Ni/Co-MOF-reduced graphene oxide nanocomposite as a high performance supercapacitor electrode material, *Electrochim. Acta*, 2018, **275**, 76-86.
43. M. Gao, W. Sheng, Z. Zhuang, Q. Fang, S. Gu, J. Jiang and Y. Yan, Efficient water oxidation using nanostructured α-nickel-hydroxide as an electrocatalyst, *J. Am. Chem. Soc.*, 2014, **136**, 7077-7084.
44. D. K. Bediako, B. Lassalle-Kaiser, Y. Surendranath, J. Yano, V. K. Yachandra and D. G. Nocera, Structure–activity correlations in a nickel–borate oxygen evolution catalyst, *J. Am. Chem. Soc.*, 2012, **134**, 6801-6809.
45. Y. J. Leem, K. Cho, K. H. Oh, S. H. Han, K. M. Nam and J. Chang, A self-assembled Ni (cyclam)-BTC network on ITO for an oxygen evolution catalyst in alkaline solution, *Chem. Commun.*, 2017, **53**, 3454-3457.
46. N. Padmanathan, H. Shao and K. M. Razeeb, Multifunctional nickel phosphate nano/microflakes 3D electrode for electrochemical energy storage, nonenzymatic glucose, and sweat pH sensors, *ACS Appl. Mater. Interfaces*, 2018, **10**, 8599.

47. P. T. Toi, T. Q. Trung, T. M. L. Dang, C. W. Bae and N. E. Lee, Highly electrocatalytic, durable, and stretchable nanohybrid fiber for on-body sweat glucose detection, *ACS Appl. Mater. Interfaces*, 2019, **11**, 10707-10717.
48. X. Xuan, H. S. Yoon and J. Y. Park, A wearable electrochemical glucose sensor based on simple and low-cost fabrication supported micro-patterned reduced graphene oxide nanocomposite electrode on flexible substrate, *Biosens. Bioelectron.*, 2018, **109**, 75-82.
49. Y. Wang, X. Wang, W. Lu, Q. Yuan, Y. Zheng and B. Yao, A thin film polyethylene terephthalate (PET) electrochemical sensor for detection of glucose in sweat, *Talanta*, 2019, **198**, 86-92.
50. Q. Huang, K. Zhang, Y. Yang, J. Ren, R. Sun, F. Huang and X. Wang, Highly smooth, stable and reflective Ag-paper electrode enabled by silver mirror reaction for organic optoelectronics, *Chem. Eng. J.*, 2019, **370**, 1048-1056.
51. S. Huang, F. Wan, S. Bi, J. Zhu, Z. Niu and J. Chen, A self-healing integrated all-in-one zinc-ion battery, *Angew. Chem. Int. Ed. Engl.*, 2019, **58**, 4313-4317.
52. J. Yang, P. Xiong, C. Zheng, H. Qiu and M. Wei, Metal–organic frameworks: a new promising class of materials for a high performance supercapacitor electrode, *J. Mater. Chem. A*, 2014, **2**, 16640-16644.
53. L. Zhang, Y. Zhang, S. Huang, Y. Yuan, H. Li, Z. Jin, J. Wu, Q. Liao, L. Hu and J. Lu, Co3O4/Ni-based MOFs on carbon cloth for flexible alkaline battery-supercapacitor hybrid devices and near-infrared photocatalytic hydrogen evolution, *Electrochim. Acta*, 2018, **281**, 189-197.
54. J. Yang, C. Zheng, P. Xiong, Y. Li and M. Wei, Zn-doped Ni-MOF material with a high supercapacitive performance, *J. Mater. Chem. A*, 2014, **2**, 19005-19010.
55. Z. Sun, X. Jiang, Q. Wen, W. Li and H. Zhang, Single frequency fiber laser based on an ultrathin metal–organic framework, *J. Mater. Chem. C*, 2019, **7**, 4662-4666.
56. A. Carton, A. Mesbah, T. Mazet, F. Porcher and M. François, Ab initio crystal structure of nickel (II) hydroxy-terephthalate by synchrotron powder diffraction and magnetic study, *Solid State Sci.*, 2007, **9**, 465-471.
57. M. Q. Wang, Y. Zhang, S. J. Bao, Y. N. Yu and C. Ye, Ni (II)-based metal-organic framework anchored on carbon nanotubes for highly sensitive non-enzymatic hydrogen peroxide sensing, *Electrochim. Acta*, 2016, **190**, 365-370.
58. H. Zou, D. Tian, C. Lv, S. Wu, G. Lu, Y. Guo, Y. Liu, Y. Yu and K. Ding, The synergistic effect of Co/Ni in ultrathin metal–organic framework nanosheets for the prominent optimization of non-enzymatic electrochemical glucose detection, *J. Mater. Chem. B*, 2020, **8**, 1008-1016
59. X. Liu, L. Zhang, X. Gao, C. Guan, Y. Hu and J. Wang, Enlarged interlayer spacing in cobalt-manganese layered double hydroxide guiding transformation to layered structure for high supercapacitance, *ACS Appl. Mater. Interfaces*, 2019, **11**, 23236-23243.
60. Y. Liu, L. Guo, X. Teng, J. Wang, T. Hao, X. He and Z. Chen, High-performance 2.5 V flexible aqueous asymmetric supercapacitors based on K^+/Na^+-inserted MnO_2 nanosheets, *Electrochim. Acta*, 2019, **300**, 9-17.
61. T. Deng, W. Zhang, O. Arcelus, D. Wang, X. Shi, X. Zhang, J. Carrasco, T. Rojo and W. Zheng, Vertically co-oriented two dimensional metal-organic frameworks for packaging enhanced supercapacitive performance, *Commun. Chem.*, 2018, **1**, 6.
62. E. Shangguan, J. Li, D. Guo, L. Guo, M. Nie, Z. Chang, X. Yuan and H. Wang, A comparative study of structural and electrochemical properties of high-density aluminum substituted α-nickel hydroxide containing different interlayer anions, *J. Power Sources*, 2015, **282**, 158-168.
63. J. Huang, D. Cao, T. Lei, S. Yang, X. Zhou, P. Xu and G. Wang, Structural and electrochemical performance of Al-substituted β-$Ni(OH)_2$ nanosheets electrodes for nickel metal hydride battery, *Electrochim. Acta*, 2013, **111**, 713-719.
64. H. Huang, Y. Guo and Y. Cheng, Ultrastable α phase nickel hydroxide as energy storage materials for alkaline secondary batteries, *Appl. Surf. Sci.*, 2018, **435**, 635-640.
65. Y. Wang, D. Cao, G. Wang, S. Wang, J. Wen and J. Yin, Spherical clusters of β-Ni(OH)2 nanosheets supported on nickel foam for nickel metal hydride battery, *Electrochim. Acta*, 2011, **56**, 8285-8290.
66. X. Han, P. Xu, C. Xu, L. Zhao, Z. B. Mo and T. Liu, Study of the effects of nanometer β-Ni(OH)2 in nickel hydroxide electrodes, *Electrochim. Acta*, 2005, **50**, 2763-2769.
67. Y. Shao, M. F. El-Kady, J. Sun, Y. Li, Q. Zhang, M. Zhu, H. Wang, B. Dunn and R. B. Kaner, Design and Mechanisms of Asymmetric Supercapacitors, *Chem. Rev.*, 2018, **118**, 9233-9280.
68. S. K. Hassaninejaddarzi, Fabrication of a non-enzymatic Ni(II) loaded ZSM-5 nanozeolite and multi-walled carbon nanotubes paste electrode as a glucose electrochemical sensor, *RSC Adv.*, 2015, **5**, 105707-105718.
69. J. Chen, X. Zheng, Y. Li, H. Zheng, Y. Liu and S.-I. Suye, A glucose biosensor based on direct electron transfer of glucose oxidase on PEDOT modified microelectrode, *J. Electrochem. Soc.*, 2020, **167**, 067502.
70. S. K. Hassaninejaddarzi and M. Gholamiesfidvajani, Preparation of nanoporous nickel phosphate VSB-5 nanorods carbon paste electrode as glucose non-enzymatic sensor, *J. Porous Mater.*, 2017, **24**, 85-95.
71. S. Ammara, S. Shamaila, A. Bokhari and A. Sabah, Nonenzymatic glucose sensor with high performance electrodeposited nickel/copper/carbon nanotubes nanocomposite electrode, *J. Phys. Chem. Solids*, 2018, **120**, 12-19.
72. S. N. Azizi, S. Ghasemi and H. Yazdanisheldarrei, Synthesis of mesoporous silica (SBA-16) nanoparticles using silica extracted from stem cane ash and its application in electrocatalytic oxidation of methanol, *Int. J. Hydrogen Energy*, 2013, **38**, 12774-12785.

Graphical Contents Entry

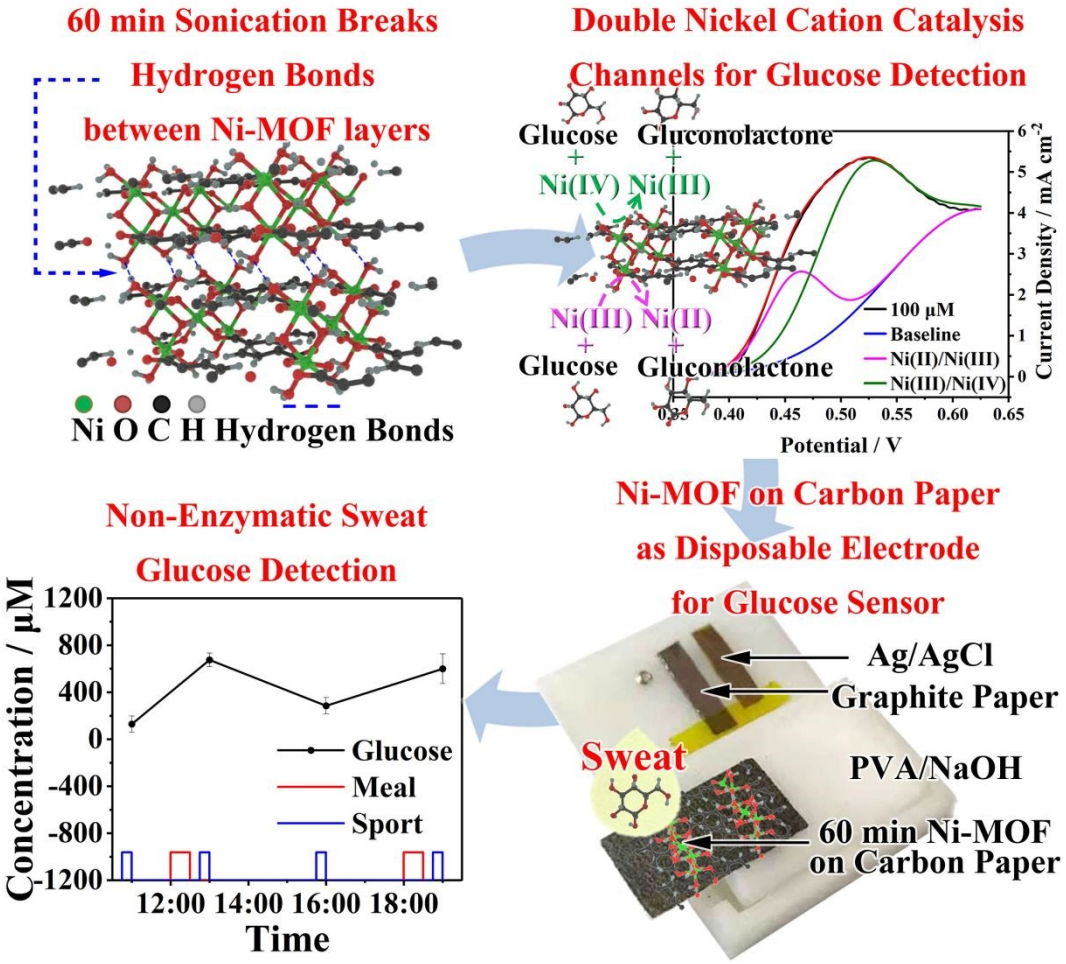

Longitudinally expanded Ni-Based metal-organic framework with enhanced double nickel cation catalysis reaction channels was used for non-enzymatic sweat glucose biosensor.